



# Response of pore network fractal dimensions and gas adsorption capacities of shales exposed to supercritical CO<sub>2</sub>: Implications for CH<sub>4</sub> recovery and carbon sequestration



Shaoqiu Wang<sup>a,b</sup>, Sandong Zhou<sup>a,b,\*</sup>, Zhejun Pan<sup>c</sup>, Derek Elsworth<sup>d</sup>, Detian Yan<sup>a</sup>, Hua Wang<sup>a</sup>, Dameng Liu<sup>e</sup>, Zhazha Hu<sup>f</sup>

<sup>a</sup> Key Laboratory of Tectonics and Petroleum Resources of the Ministry of Education, China University of Geosciences, Wuhan 430074, PR China

<sup>b</sup> School of Earth Resources, China University of Geosciences, Wuhan 430074, PR China

<sup>c</sup> Key Laboratory of Continental Shale Hydrocarbon Accumulation and Efficient Development, Ministry of Education, Northeast Petroleum University, Daqing, Heilongjiang, 163318, PR China

<sup>d</sup> Department of Energy and Mineral Engineering, G3 Centre and Energy Institute, The Pennsylvania State University, University Park, PA 16802, USA

<sup>e</sup> Coal Reservoir Laboratory of National Engineering Research Center of CBM Development & Utilization, School of Energy Resources, China University of Geosciences, Beijing 100083, PR China

<sup>f</sup> School of Energy Science and Engineering, Henan Polytechnic University, 454003 Jiaozuo, PR China

## ARTICLE INFO

### Article history:

Received 24 October 2022

Received in revised form 10 March 2023

Accepted 30 May 2023

Available online xxx

### Keywords:

Shales  
Supercritical CO<sub>2</sub>  
Fractal dimension  
Adsorption capacity  
Carbon geological sequestration

## ABSTRACT

The injection of CO<sub>2</sub> into shale reservoirs potentially increases rates and masses of CH<sub>4</sub> recovery and simultaneously contributes to the sequestration of CO<sub>2</sub>. At typical reservoir conditions (T ≥ 31.08 °C, P ≥ 7.38 MPa) the CO<sub>2</sub> will be supercritical. We compile, analyze, and supplement experimental data of shales from several basins across China, and use X-ray diffraction, scanning electron microscopy and low-pressure gas adsorption to characterize variations in shale pore structure before and after supercritical CO<sub>2</sub> (ScCO<sub>2</sub>) treatment, and supplement these with CH<sub>4</sub>/CO<sub>2</sub> adsorption experiments to characterize changes in shale adsorption capacity. The results show that clay and carbonate contents significantly decrease, and the relative content of quartz is increased after ScCO<sub>2</sub> treatment. Pore structure changes significantly after ScCO<sub>2</sub> treatment, with the majority of the shales showing a decrease in total specific surface area and total pore volume and an increase in average pore size – indicating the transformation of some micropores and smaller mesopores into mesopores and macropores. After ScCO<sub>2</sub> treatment, the experimentally derived absolute adsorption volumes of both CH<sub>4</sub> and CO<sub>2</sub> decrease, and the volumes of both CH<sub>4</sub> and CO<sub>2</sub> fitting a Langmuir isotherm decrease with an increase in treatment pressure and increase with an increase in temperature. The adsorption selectivity factors  $\alpha_{\text{CO}_2/\text{CH}_4}$  all remain greater than 1 with  $\alpha_{\text{CO}_2/\text{CH}_4}$  primarily controlled by the pore structure. The fractal dimension is positively correlated with Langmuir volume and negatively correlated with Langmuir pressure while the fractal dimensions are negatively correlated with  $\alpha_{\text{CO}_2/\text{CH}_4}$ . The selectivity factor  $\alpha_{\text{CO}_2/\text{CH}_4}$  decreases rapidly above a fractal dimension threshold (D1 > 2.65, D2 > 2.80). This paper further reveals critical interactions between ScCO<sub>2</sub> and shale and defines controls on and of pore structure and adsorption capacity to speculate on physical and chemical storage mechanisms of CO<sub>2</sub> in shale reservoirs. This provides several theoretical bases for shale gas recovery and the sequestration of CO<sub>2</sub>.

© 2023 The Author(s). Published by Elsevier Ltd. This is an open access article under the CC BY-NC-ND license (<http://creativecommons.org/licenses/by-nc-nd/4.0/>).

## 1. Introduction

Currently, oil and natural gas remain the majority fuels in the world energy market, accounting for more than 55% of total

energy consumption (Cheng et al., 2020; Dai et al., 2020; Fatah et al., 2022a). The increase in energy demand and the broad availability of unconventional energy sources (for example, coalbed methane, shale gas and tight oil) has driven an interest in effective methods for their recovery (Li et al., 2020a; Zhao et al., 2022a), as well as the implementation of the “Dual Carbon Goal”, the trend of low carbon and energy decarbonization is gradually strengthening (Zou et al., 2021, 2022). Shale gas extraction has been enabled by technological advancements in horizontal drilling and multi-stage hydraulic fracturing (Norman, 1974;

\* Corresponding author at: Key Laboratory of Tectonics and Petroleum Resources of the Ministry of Education, China University of Geosciences, Wuhan 430074, PR China.

E-mail address: [zhousandong@cug.edu.cn](mailto:zhousandong@cug.edu.cn) (S. Zhou).

Wang and Krupnick, 2015), although environmental challenges remain. These relate to consumptive water use, fugitive emissions in the subsurface and atmosphere and the increase in levels of induced seismicity (Thomas et al., 2017). These issues have driven investigations into non-aqueous fluids for hydraulic fracturing (Yang et al., 2020), including CO<sub>2</sub> as an environmentally benign, and indeed beneficial, substitute (Mastalerz et al., 2009). Experiments and theory indicate that CH<sub>4</sub> has a lower adsorption affinity than CO<sub>2</sub> in shale ((Busch et al., 2003; Duan et al., 2016; Li et al., 2020b). Thus, competitive desorption can be used to both preferentially liberate CH<sub>4</sub> and sequester CO<sub>2</sub> – referred to as CO<sub>2</sub> enhanced shale gas recovery (CO<sub>2</sub>-ESGR) with geological sequestration (Liu et al., 2020; Lu et al., 2021; Mastalerz et al., 2009; Rogala et al., 2014; Zhou et al., 2019a, 2022b).

The microstructure of shale can be significantly altered after exposure to supercritical CO<sub>2</sub> (ScCO<sub>2</sub>) (Cheng et al., 2020; Fatah et al., 2022a; Hui et al., 2019; Pan et al., 2018a; Sanguinito et al., 2018). Key observed features of this impact are: (1) ScCO<sub>2</sub> treatment has limited impact on the basic pore morphology of macropores but more significant effects on micropores (Yin et al., 2016; Zhao et al., 2022b); (2) After ScCO<sub>2</sub> treatment, the pore structure complexity and pore surface roughness of marine shale were significantly reduced. Compared with lacustrine shale, the microstructure of marine shale is more easily affected by ScCO<sub>2</sub> (Pan et al., 2018a; Yang et al., 2022a); (3) Increasing specific surface area and porosity with time and pressure, the magnitude of pressure exerting a greater effect on changes in the microstructure of shale. At lower pressure (< 8 MPa), the treatment of ScCO<sub>2</sub> at different temperatures had no significant effect on the microstructure of the shale (Jiang et al., 2016); (4) The effect of ScCO<sub>2</sub> on the microstructure of layering was more significant than that on the matrix in shale; ScCO<sub>2</sub> primarily enlarged micropores in the matrix, converting them into mesopores and macropores in the vicinity of bedding planes (Bai et al., 2021). However, we note some omissions in these varied observations. Conclusions drawn from relatively limited data, sometimes reflected in a sole sampling location per type-shale and limited samples of lacustrine shales relative to marine shales. Thus, the following add multiple sets of experimental observations, including marine and lacustrine samples from different regions, to bolster the representativeness of experimental conclusions.

Shale gas is mainly stored in the fractures and pores in adsorbed, free, and dissolved states, with adsorbed gas contents typically reaching 20% to 85% of total gas contents (Curtis, 2002; Etminan et al., 2014; Hu et al., 2021a; Sondergeld et al., 2010). With such significant proportions adsorbed, changes in adsorption capacity resulting from ScCO<sub>2</sub> exposure is an important direction of study. The adsorption capacity of CO<sub>2</sub> and CH<sub>4</sub> is primarily influenced by shale reservoir conditions (in situ stress, moisture, temperature, and pressure) and rock properties (TOC, maturity, kerogen type, mineral content, and pore structures) (Duan et al., 2016; Fatah et al., 2022a; Gasparik et al., 2014; Klewiah et al., 2020). An analysis of the multiple factors affecting the adsorption capacity demonstrates a positive correlation between shale CH<sub>4</sub> adsorption capacity and TOC, quartz content, specific surface area (Niu et al., 2018). Generally, the CO<sub>2</sub> adsorption capacity of shale far exceeds the CH<sub>4</sub> sorption capacity, and the selectivity factor  $\alpha_{\text{CO}_2/\text{CH}_4}$  is mainly controlled by the moisture, type of shale (according to the sedimentary environment) and pore structure (Duan et al., 2016; Lan et al., 2019; Yin et al., 2016). It is worth noting that current gas sorption experiments are primarily conducted on crushed samples at different pore pressures by using manometric or gravimetric methods, which are both fast and convenient. However, an obvious limitation is an uncertainty of whether these data can reflect the sorption capacity of intact shale under in-situ conditions. In addition, related

studies have been conducted primarily using single-component adsorbents, while fewer experiments have been conducted on shale with CO<sub>2</sub>/CH<sub>4</sub> gas mixtures.

Mechanisms of ScCO<sub>2</sub>-shale interactions indicate that after the reaction of the shale with a mixture of brine and ScCO<sub>2</sub> under different temperature and pressure conditions, carbonate-rich are more active than clay-rich shales – with clay-rich shales showing no significant mineralogical changes except for the dissolution of silicate minerals (Alemu et al., 2011). Shale microstructure is typically affected by the ScCO<sub>2</sub> treatment pressure, temperature, and time. The mechanism is mainly the release of bound water from clay minerals after treatment and the increase of porosity and specific surface area with the increase of exposure pressure and time (Jiang et al., 2016). After the ScCO<sub>2</sub> treatment, the water interfacial contact angle on shale surfaces increases and the treatment pressure and time are the main influencing factors – with temperature exerting little effect (Qin et al., 2016). Mercury injection porosimetry (MIP) and nuclear magnetic resonance (NMR) spectroscopy show a decrease in capillary entry pressure and an increase in pore volume for most samples with ScCO<sub>2</sub> treatment (Qin et al., 2016; Rezaee et al., 2017). The interplay among energies of adsorbents (N<sub>2</sub>, CH<sub>4</sub>, and CO<sub>2</sub>) and micropores of different widths have been characterized using a slit-shaped pore model by Cui et al. (2004). In summary, the microstructure, relative fractions of organic matter and mineral contents of shales are changed by the interplay between ScCO<sub>2</sub> and shale. The gas adsorption capacity is directly related to the micropore structure (size, distribution, and connectivity) and clay mineral contents of shales. Thus, the following explores the effect of microstructural changes on the adsorption capacity of shale under the action of ScCO<sub>2</sub>. In addition, due to the high heterogeneity of shale, the response mechanisms of different shale samples from similar locales/types to exposure to ScCO<sub>2</sub> are different. Thus, the effects of ScCO<sub>2</sub> on the evolving microstructure and gas adsorption capacity of different types of shales require quantification – with due regard to the initial key characteristics.

Sorption mechanisms and interactions within the CO<sub>2</sub>-ESGR are multiple and coupled. Among them, the contributions of variations in mineralogy, pore structure and heterogeneity in adsorption capacity are key components that are strongly interconnected with important mechanistic feedback. Fig. 1 illustrates the workflow of this paper of prevailing and new observations. Through a series of research processes, we: (1) Characterize the microstructural alterations resulting from ScCO<sub>2</sub> exposure; (2) Probe key mechanisms and influencing factors on changes in adsorption capacity that result from ScCO<sub>2</sub> exposure, including the key role of fractal dimension on the selectivity factor; (3) Summarize the mechanisms representing the interplay between ScCO<sub>2</sub> and shale. Finally, guidance is provided to evaluate the adaptability of CO<sub>2</sub>-ESGR to various shale gas reservoirs.

## 2. Experimental methods

### 2.1. Sample preparation

We recover marine shale samples from the Longmaxi and Wufeng formations of the Sichuan Basin (M1–M21) and lacustrine shales from the Shahezi formation of the Songliao Basin and the Yanchang formation of the Ordos Basin (L1–L22), China. All samples are crushed and sieved in the 60–200 μm particle fraction, with each sample divided into two subsamples (Cheng et al., 2020). The types, mineral composition, and pore structure parameters of samples are shown in Table 1.

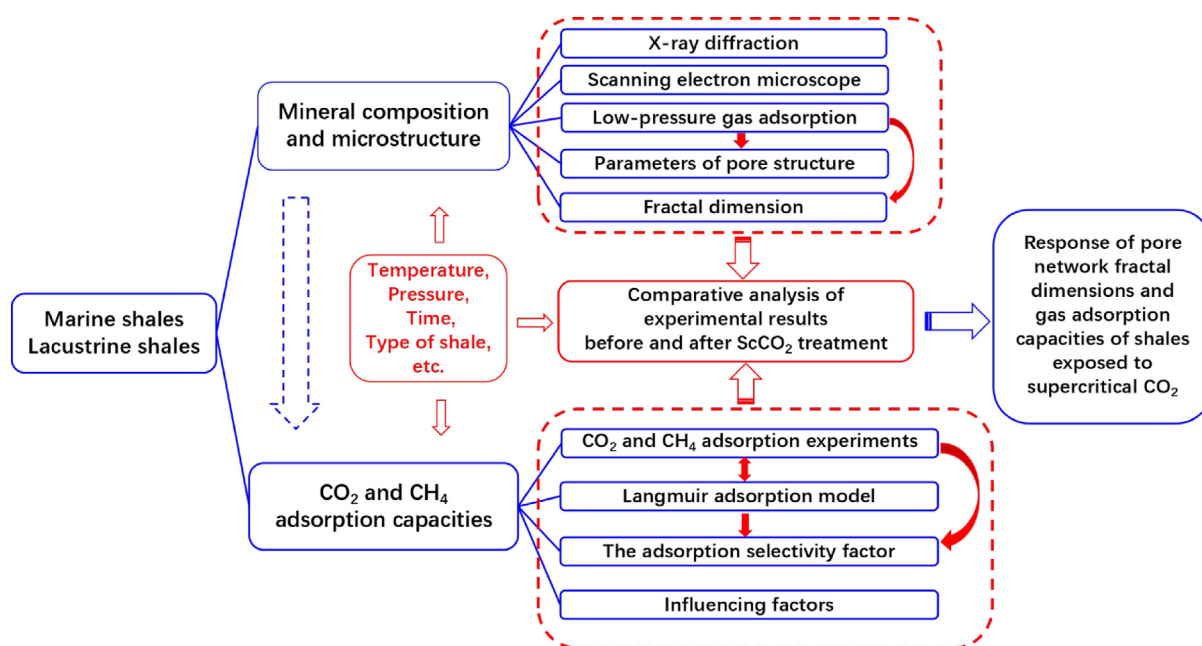


Fig. 1. Research workflow.

## 2.2. ScCO<sub>2</sub> exposure

The ScCO<sub>2</sub> treatment system consists of a CO<sub>2</sub> gas supply, a gas-compression pump, and a high-pressure reactor. Based on the depth and geothermal gradient for principal shale reserves in each shale source area, appropriate temperature and pressure are set to simulate the in-situ environment – representative of supercritical conditions for the CO<sub>2</sub>. The equilibrium and reaction times are fully considered to determine appropriate exposure times of ScCO<sub>2</sub> and to allow reactions and sorption to complete. At the conclusion of the treatment, the high-pressure reactor is depressurized, and the samples are removed and stored in polyethylene bags to retain representative humidities. In the experiments, each sample is crushed and divided into two equivalent subsamples, one of which is treated using ScCO<sub>2</sub> and the other sample left untreated as a control sample to better determine the effect of ScCO<sub>2</sub> treatment on pore structure and adsorption capacity.

## 2.3. X-ray diffraction

The determination of mineral composition of shale samples mainly adopts X-ray diffraction method, which has been widely used in the quantitative characterization of rock mineral composition (Hu et al., 2021a; Li et al., 2020a). The general steps are as follows: (1) Particles larger than 400 μm are gently crushed in a mortar with added 0.2 g/g of Baikowski α-Al<sub>2</sub>O<sub>3</sub>. (2) A McCrone micronizing mill is used for 15 min with ethanol as a coolant to avoid excessive strain, thermal damage, and mineral dissolution. (3) XRD powder patterns are measured on the X-ray diffractometer using Cu Kα radiation (40 kV, 40 mA). Mineralogical alterations of the shale samples are measured using a Shimadzu XRD 6000 X-ray diffractometer (Japan).

## 2.4. Scanning electron microscopy

SEM provides high-resolution images to observe the evolution of microstructures at the nanoscale. First, the surface morphology of the samples before ScCO<sub>2</sub> treatment was characterized by high-resolution SEM. Subsequently, to observe changes in shale

surface morphology in the same field of view, the ScCO<sub>2</sub>-treated samples are accurately re-positioned and re-imaged. The surface morphology analysis in this paper is conducted by a JSM-7800F FE-SEM instrument (JEOL, Japan).

## 2.5. Low-pressure CO<sub>2</sub> and N<sub>2</sub> adsorption

Low-pressure CO<sub>2</sub> and N<sub>2</sub> adsorption measure adsorption (CO<sub>2</sub> and N<sub>2</sub> molecules) onto the adsorbent (shale) and enable the evaluation of the adsorbent pore structure – recovered using the amount of adsorption as a proxy. The micropore and mesopore structures are analyzed using CO<sub>2</sub> and N<sub>2</sub> adsorption, respectively. In this paper, the isotherms of CO<sub>2</sub> and N<sub>2</sub> adsorption are from an Autosorb IQ2 adsorption analyzer (Quantachrome Instrument Corporation, American) and an ASAP-2460 adsorption analyzer (Micromeritics Instruments, America), respectively (Li et al., 2017a).

## 2.6. CH<sub>4</sub> and CO<sub>2</sub> adsorption

The manometric method investigates the gas adsorption with ScCO<sub>2</sub> treatment (Hu, 2018; Liu, 2017). This system (Hu, 2018; Liu, 2017) consists of sample chamber, reference chamber, switching valves, high-pressure gas cylinder, plunger pump, pipeline, pressure sensor and vacuum pump. The experimental procedure is: (I) The samples are ground into powder and dried to remove water. (II) The shale samples are completely degassed by applying a vacuum. (III) Isothermal adsorption experiments of CH<sub>4</sub> then CO<sub>2</sub> are conducted separately and successively, with the adsorption temperature set to 35 °C, 45 °C, 55 °C, the pressure set to 0–15 MPa.

## 3. Microstructural impacts

Two major factors lead to shale microstructural alterations after ScCO<sub>2</sub> exposure: (I) Swelling effects caused by shale adsorption of ScCO<sub>2</sub>. (II) Dissolution of minerals by ScCO<sub>2</sub> (Huang et al., 2019; Pan et al., 2018a; Rezaee et al., 2017). Currently, various methods are widely used to characterize the microstructure of rocks, including XRD, SEM (Yin et al., 2016), nuclear magnetic

**Table 1**

Types, geochemical data, and mineral compositions of the shale samples.

Source: Data from Cheng et al. (2020), Hu (2018), Hui et al. (2019), Li et al. (2022), Liu (2017), Pan et al. (2018a,b), Yang et al. (2022a).

Sample	Types	Total organic carbon (%)	Mineral compositions (%)		Total specific surface area (m <sup>2</sup> /g)	Total pore volume (cm <sup>3</sup> /g)	Average pore size (nm)
			Quartz	Clay minerals			
M1	Marine	3.72	46.00	31.90	19.690	0.0261	9.19
M2	Marine	3.64	57.10	22.30	20.410	0.0238	8.33
M3	Marine	3.12	45.40	15.40	18.850	0.0220	8.43
M4	Marine	3.77	44.00	28.60	24.640	0.0297	8.19
M5	Marine	2.58	58.80	29.60	15.110	0.0237	8.98
M6	Marine	2.50	58.60	35.30	18.440	0.0262	8.74
M7	Marine	3.24	43.20	27.30	22.540	0.0173	3.07
M8	Marine	2.98	46.80	24.80	20.900	0.0180	3.44
M9	Marine	4.18	41.10	28.90	25.330	0.0215	3.39
M10	Marine	3.45	40.20	30.80	26.870	0.0239	3.55
M11	Marine	0.67	41.40	48.20	7.790	0.0072	6.11
M12	Marine	3.81	62.39	19.99	20.669	0.0410	N/A
M13	Marine	2.05	39.78	9.28	10.274	0.0170	7.24
M14	Marine	4.02	57.38	24.88	20.717	0.0290	7.12
M15	Marine	3.67	55.53	28.00	17.561	0.0290	8.52
M16	Marine	1.96	38.24	9.86	8.539	0.0160	9.30
M17	Marine	3.66	34.00	29.60	17.850	0.0245	6.62
M18	Marine	3.69	42.40	8.90	18.970	0.0148	6.12
M19	Marine	4.27	53.30	19.50	19.660	0.0150	6.16
M20	Marine	5.14	49.50	11.50	19.340	0.0152	6.11
M21	Marine	3.89	49.20	18.70	10.050	0.0079	6.89
M22	Marine	4.51	55.10	20.60	28.970	0.0233	5.99
M23	Marine	4.49	55.80	26.90	28.070	0.0239	6.11
M24	Marine	1.05	41.10	14.30	16.170	0.0160	6.27
M25	Marine	3.71	42.60	8.70	18.950	0.0146	6.14
M26	Marine	5.15	49.40	11.60	19.360	0.0153	6.13
M27	Marine	1.06	41.20	14.20	16.190	0.0162	6.29
L1	lacustrine	1.44	39.38	46.59	5.832	0.0187	12.86
L2	lacustrine	0.82	28.35	53.37	5.611	0.0178	12.67
L3	lacustrine	2.07	36.22	40.70	2.849	0.0079	11.12
L4	lacustrine	0.75	23.66	37.85	4.561	0.0124	10.89
L5	lacustrine	0.67	38.01	31.32	2.558	0.0076	11.81
L6	lacustrine	1.10	31.28	48.66	4.756	0.0117	9.87
L7	lacustrine	2.51	37.79	34.26	3.068	0.0077	10.01
L8	lacustrine	0.43	58.89	40.21	5.106	0.0130	10.21
L9	lacustrine	1.93	31.50	57.83	4.028	0.0127	12.63
L10	lacustrine	0.66	26.95	63.17	3.840	0.0167	17.44
L11	lacustrine	3.49	34.58	54.13	2.796	0.0088	12.63
L12	lacustrine	2.40	25.86	44.04	8.03	0.0164	8.17
L13	lacustrine	1.02	32.53	56.11	5.626	0.0111	7.91
L14	lacustrine	1.17	31.39	57.94	6.834	0.0133	7.81
L15	lacustrine	1.68	32.19	49.91	7.298	0.0122	6.70
L16	lacustrine	1.23	31.91	56.16	6.816	0.0118	6.95
L17	lacustrine	2.67	23.26	47.49	8.834	0.0380	N/A
L18	lacustrine	5.64	23.61	47.35	9.234	0.0260	8.43
L19	lacustrine	4.32	26.63	34.32	6.688	0.0240	10.07
L20	lacustrine	5.81	15.64	48.20	5.589	0.0240	12.58
L21	lacustrine	3.19	28.90	35.80	1.470	0.0069	18.69
L22	lacustrine	3.18	28.80	36.10	1.480	0.0071	18.69

N/A = No Data.

resonance (NMR) (Sondergeld et al., 2013), low-pressure CO<sub>2</sub> and N<sub>2</sub> adsorption (Cheng et al., 2020; Nie et al., 2015), mercury injection porosimetry (MIP) (Daniel and Kaldi, 2012), ultra-small angle and small angle neutron scattering, together with ultra-small angle, small angle and wide angle X-ray scattering tests (Sun et al., 2020).

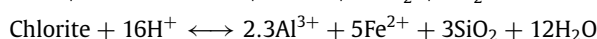
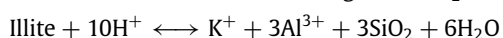
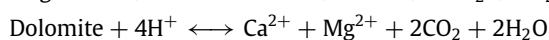
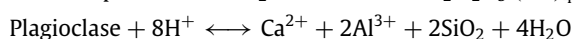
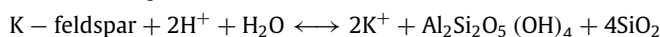
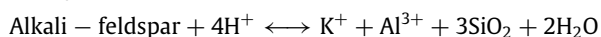
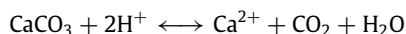
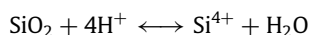
### 3.1. Mineralogical alterations

In order to ascertain the alteration of the shale with ScCO<sub>2</sub> treatment, the mineral composition before and after treatment is first measured. XRD, Neutron diffraction, electron diffraction, infrared spectroscopy, Mossbauer spectroscopy and other methods are used to analyze and determine the composition of relevant minerals. Among them, XRD is one of the most effective and widely used methods. Nevertheless, XRD remains a semi-quantitative method, subtle variations in the content of several

shale minerals are not accurately described as a consequence of sample heterogeneity (Gu et al., 2018; Pan et al., 2018a).

Quartz, clay minerals, feldspar, calcite, pyrite, and dolomite are the main components of shale, whereas clay minerals include illite, chlorite, kaolinite, and montmorillonite (Huang et al., 2017; Wang et al., 2012). The mineral composition of marine shales is similar to that of lacustrine shales, but there are significant differences in mineral proportions (Fatah et al., 2022a; Jiang et al., 2016; Pan et al., 2018b). Marine shales are rich in quartz and poor in clay minerals, while lacustrine shales are rich in clay minerals and relatively poor in quartz (Sun et al., 2022; Yang et al., 2022b). The relative mineral compositions of marine and lacustrine shales are changed to different extents following ScCO<sub>2</sub> treatment, with a significant increase in the relative content of unreactive quartz and a decrease in the contents of reactive carbonates and clay minerals. A particularly pronounced decrease is detected in the content of carbonate. Experimental observations

confirm significant dissolution in shale. However, quartz is essentially unreactive with CO<sub>2</sub>, with the decrease in the total mass of other shale minerals reacting with ScCO<sub>2</sub> being the principal reason for the increase in relative quartz content (Yin et al., 2016). Studies on the chemical reactions among shale, brine and CO<sub>2</sub> identify that the rapid reaction of shale with supercritical CO<sub>2</sub> is mainly related to the presence of H<sup>+</sup> (Cheng et al., 2020; Fatah et al., 2021; Sanguinito et al., 2018). CO<sub>2</sub> dissolves into the water film in the pores of the shale and produces carbonic acid, which triggers a series of reversible chemical reactions (Ao et al., 2017; Dai et al., 2020; Fatah et al., 2021; Kweon and Deo, 2017; Pan et al., 2018a; Rezaee et al., 2017):



Controlling the ScCO<sub>2</sub> treatment conditions on shale shows that the clay mineral and carbonate contents decrease and quartz content increases as the treatment temperature increases and the pressure decreases (Yang et al., 2022a). This is primarily due to the solubility of CO<sub>2</sub> in water decreasing and the pH of the solution increasing as the temperature increases and the pressure decreases (Deng et al., 2018; Peng et al., 2013). The stronger the solubility of the CO<sub>2</sub>-water solution and the lower the pH, the stronger the reaction and dissolution of several inorganic minerals in the shale, which leads to the alteration of quartz, clay, and carbonate mineral contents.

It is noteworthy that the conceptualization of the mineralization capture mechanism is still at a preliminary stage compared to our understanding of the adsorption capture mechanism (Fatah et al., 2022a; Pan et al., 2018a; Schaef et al., 2014a) with the effects of exposure time scale and in understanding the impacts of deep brines remaining key challenges. Future studies should combine numerical simulations and consider the influence of concentrated brines on the reactions to constrain further mineral chemical reactions under the influence of multiple factors and for extended time scales.

### 3.2. Pore structure alterations

#### 3.2.1. Surface morphology

The variations in samples' macropore structure and surface morphology are usually analyzed by SEM. SEM techniques aid in understanding the pore structure system in shale – but limitations remain in the characterization of micropores (Das et al., 2021; Hu et al., 2021a,b; Nie et al., 2015; Yin et al., 2016). SEM microscopy is performed for the same split samples of powdered shale both before and after ScCO<sub>2</sub> treatment to observe the alterations in the microscopic surfaces of the pores.

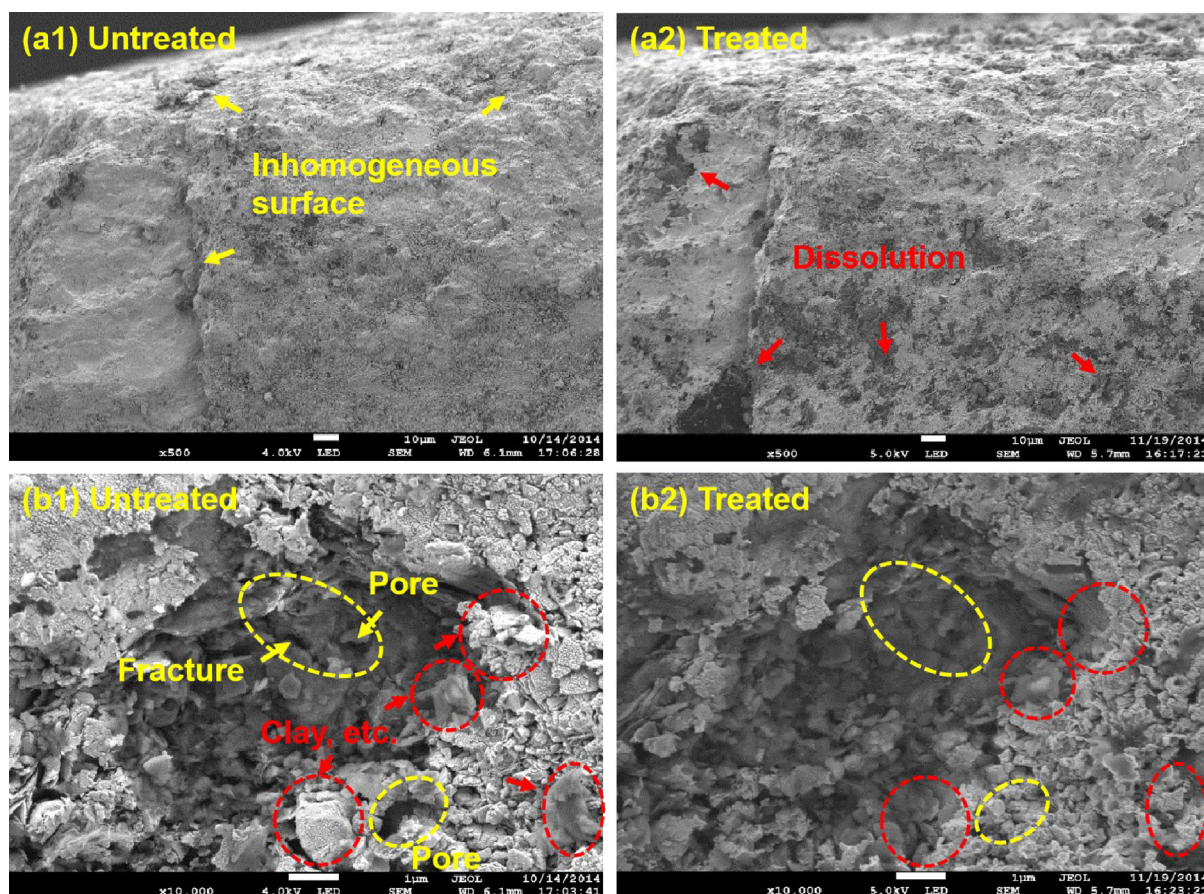
The distribution of quartz, clay and carbonate minerals on shale surface is highly heterogeneous (Fig. 2a1, a2) (Pan et al., 2018a). SEM images of marine shale, before and then after ScCO<sub>2</sub> treatment are illustrated in Fig. 2, where a few pores and fractures are narrowed due to CO<sub>2</sub> adsorption-induced swelling (Fig. 2b1, b2, yellow dotted circle area) (Chen et al., 2015; Lu et al., 2016), portions of minerals inhabiting the shale surface disappeared after ScCO<sub>2</sub> treatment (Fig. 2b1, b2, red dotted circle area), with

this variation is probably related to the solubility in ScCO<sub>2</sub> of inorganic minerals (Jarboe et al., 2015). Due to the low viscosity, low surface tension and high diffusivity of supercritical CO<sub>2</sub> (relative to conventional state CO<sub>2</sub>) (Kendall et al., 1999), it can be used as an organic solvent to extract non-polar aliphatic hydrocarbons and polycyclic aromatic hydrocarbons from shale. ScCO<sub>2</sub> is also capable of dissolving parts of inorganic minerals (Jiang et al., 2016), which may create fresh pores and microfractures, thus facilitating shale gas transport. During the interplay between ScCO<sub>2</sub> and shale, the dissolution or precipitation of shale minerals will affect the shale pore structure. In contrast, the dissolution of minerals will create fresh pores or microfractures, and the precipitation of minerals will reduce the fracture opening, thus affecting fluid transport (Lu et al., 2021). Notably, due to the high diffusivity of ScCO<sub>2</sub>, the SEM images primarily reveal variations in shale surface macropores. More variations will occur in the mesopore and micropore structures, with these variations generating secondary pores that significantly affect the storage capacity of the formation (Rezaee et al., 2017; Sondergeld et al., 2013; Zhou et al., 2018b). Low-pressure gas adsorption methods can further probe the pore structure of shale.

#### 3.2.2. Volume of CO<sub>2</sub> and N<sub>2</sub> adsorption

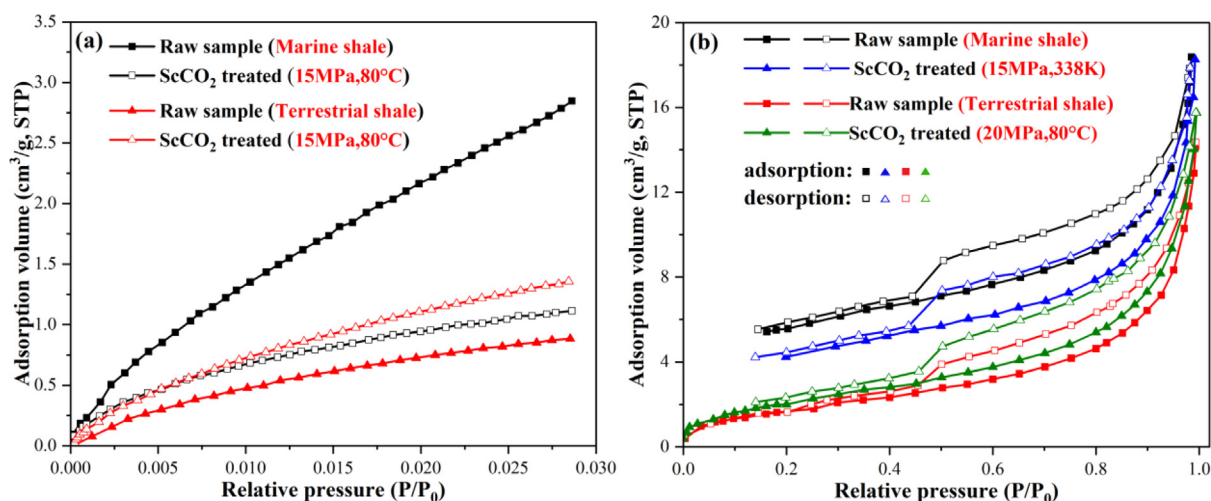
Low-pressure CO<sub>2</sub> and N<sub>2</sub> adsorption are effective methods for characterizing the shale pore structure. CO<sub>2</sub> adsorption is used to characterize changes in micropores, and N<sub>2</sub> adsorption is mainly used to characterize changes in mesopores and fine macropores (Pan et al., 2018a; Wei et al., 2016; Zhou et al., 2019b). The International Union of Pure and Applied Chemistry (IUPAC) classifies pores in shales into three categories (Orr et al., 1977; Thommes et al., 2015): micropores (<2 nm), mesopores (2–50 nm), and macropores (>50 nm).

Fig. 3 shows the adsorption isotherms for CO<sub>2</sub> and N<sub>2</sub> before and after the treatment by ScCO<sub>2</sub>. The samples' adsorption/desorption volumes are altered significantly with the ScCO<sub>2</sub> treatment. After ScCO<sub>2</sub> treatment, the CO<sub>2</sub> and N<sub>2</sub> adsorption of marine shale samples decreased, and the CO<sub>2</sub> and N<sub>2</sub> adsorption of lacustrine shale samples increased (Fig. 3a, b). The gases in shale are primarily stored in free and adsorbed states in the pores and on the rough surfaces of the minerals (Mudoi et al., 2022). Thus, the differences in the properties of marine and lacustrine shales result in different trends in adsorption after ScCO<sub>2</sub> treatment (Pan et al., 2018a). These relate to the low-pressure (P/P<sub>0</sub> = 0.05–0.45), transitional (P/P<sub>0</sub> = 0.45–0.8) and high-pressure stages (P/P<sub>0</sub> = 0.8–0.995) in the N<sub>2</sub> adsorption isotherm. The adsorption curves rise slowly and steadily in the low-pressure stage, reflecting that the N<sub>2</sub> molecules adsorbed on the shale surface are in the unimolecular adsorption state in the micropores (Pan et al., 2018b); in the transition stage, the adsorption volume increases as the pressure increases, reflecting that the nitrogen molecules gradually transition from the unimolecular state to a multilayer adsorption state; for the high-pressure stage, the adsorption volume and the slope of the curve increase dramatically – the adsorption state when the saturation vapor pressure is about to be reached is also not saturated, confirming the existence of large mesopores of shale, with this stage mainly accommodating the filling of nitrogen in large pores (Gregg et al., 1967; Qi et al., 2018). Meanwhile, a “forced closure” of the desorption curve at a relative pressure of 0.45 is observed – a process known as the tensile strength effect (Fig. 3b) (Groen et al., 2003; Pan et al., 2018b). In general, the hysteresis loop is correlated with the pore shape (the hysteresis loop is mainly explained by the capillary condensation mechanism). In previous adsorption experiments (Ao et al., 2017; Fatah et al., 2022a; Jiang et al., 2016; Yang et al., 2022a; Yin et al., 2016), it is observed that the shape of the N<sub>2</sub> isotherm hysteresis loop is not altered significantly after ScCO<sub>2</sub> treatment, indicating that ScCO<sub>2</sub> treatment has a limited effect on the pore shape of shale (Cheng et al., 2020; Fatah et al., 2022a).



**Fig. 2.** Scanning electron microscope (SEM) images of untreated (a1, b1) and ScCO<sub>2</sub> treated (a2, b2) shales. The yellow dotted line shows pores and fractures swelling then narrowing after ScCO<sub>2</sub> treatment. The red dotted line indicates that part of the material on the shale surface disappears after ScCO<sub>2</sub> treatment. (For interpretation of the references to color in this figure legend, the reader is referred to the web version of this article.)

Source: Modified from Yin et al. (2016).



**Fig. 3.** CO<sub>2</sub> (a) and N<sub>2</sub> (b) adsorption isotherm curves for shale samples both before then after ScCO<sub>2</sub> treatment. After ScCO<sub>2</sub> treatment, both CO<sub>2</sub> and N<sub>2</sub> adsorption of marine shales decreased and increased on lacustrine shales.

Source: Data from Pan et al. (2018a,b), Yang et al. (2022a).

### 3.2.3. Specific surface area and pore volume

Variations in shale pore structure after ScCO<sub>2</sub> treatment can be characterized by total specific surface area (TSSA), total pore volume (TPV) and pore size distribution (PSD). Based on CO<sub>2</sub> adsorption isotherms, the SSA and PV of the micropores are generally calculated from the Dubinin–Radushkevich (DR) and

Dubinin–Astakhov (DA) models (Rani et al., 2019). The Brunauer–Emmet–Teller (BET) and Barrett–Joyner–Halenda (BJH) models were used to calculate SSA and PV for the N<sub>2</sub> adsorption assay (Hayati-Ashtiani, 2011).

The pore structure parameters of the shale samples are altered after ScCO<sub>2</sub> exposure. The TSSA and TPV are significantly

**Table 2**Variations of shale properties and fractal dimension before and after ScCO<sub>2</sub> treatment.

Source: Data from Cheng et al. (2020), Hu (2018), Hui et al. (2019), Liu (2017), Pan et al. (2018a,b), Yang et al. (2022a).

Sample	Types	Treatment conditions	Total organic carbon (%)	Mineral compositions (%)		Total specific surface area (m <sup>2</sup> /g)	Total pore volume (cm <sup>3</sup> /g)	Average pore size (nm)	Fractal dimension D1	Fractal dimension D2
				Quartz	Clay minerals					
M7	Marine	Untreated	3.24	43.20	27.30	22.540	0.0173	3.07	2.660	2.910
		40 °C, 16 MPa, 30 days	N/A	46.30	23.70	20.470	0.0164	3.20	2.560	2.850
M8	Marine	Untreated	2.98	46.80	24.80	20.900	0.0180	3.44	2.690	2.900
		40 °C, 16 MPa, 30 days	N/A	52.20	19.90	13.600	0.0134	3.95	2.520	2.810
M9	Marine	Untreated	4.18	41.10	28.90	25.330	0.0215	3.39	2.640	2.880
		40 °C, 16 MPa, 30 days	N/A	45.20	24.30	10.000	0.0154	6.17	2.590	2.820
M10	Marine	Untreated	3.45	40.20	30.80	26.870	0.0239	3.55	2.700	2.890
		40 °C, 16 MPa, 30 days	N/A	45.40	26.70	20.540	0.0217	4.22	2.520	2.800
M11	Marine	Untreated	0.67	41.40	48.20	7.790	0.00718	6.11	2.674	2.859
		40 °C, 8 MPa, 4 days	N/A	44.50	44.70	6.350	0.00606	6.10	2.665	2.855
		50 °C, 8 MPa, 4 days	N/A	42.10	46.30	6.710	0.00646	6.17	2.665	2.856
		60 °C, 8 MPa, 4 days	N/A	40.90	47.50	7.030	0.00651	5.86	2.662	2.864
		70 °C, 8 MPa, 4 days	N/A	43.30	45.40	6.890	0.00624	5.83	2.668	2.862
		80 °C, 8 MPa, 4 days	N/A	44.40	42.40	6.720	0.00636	6.16	2.666	2.856
M12	Marine	Untreated	3.81	62.39	19.99	20.669	0.0410	N/A	2.551	2.759
		80 °C, 15 MPa, 10 days	N/A	57.05	25.04	10.550	0.0370	N/A	2.427	2.645
		80 °C, 15 MPa, 20 days	N/A	54.02	26.82	6.280	0.0300	N/A	2.448	2.565
		80 °C, 15 MPa, 30 days	N/A	52.68	20.52	6.023	0.0290	N/A	2.399	2.601
M13	Marine	Untreated	2.05	39.78	9.28	10.274	0.0170	7.24	2.426	2.782
		30 °C, 5 MPa, 14 days	N/A	40.24	9.16	8.837	0.0160	7.59	2.394	2.763
		80 °C, 20 MPa, 14 days	N/A	38.64	10.75	4.866	0.0140	9.05	2.250	2.684
M14	Marine	Untreated	4.02	57.38	24.88	20.717	0.029	7.12	2.545	2.791
		30 °C, 5 MPa, 14 days	-	55.87	27.67	16.794	0.026	8.24	2.521	2.773
		80 °C, 20 MPa, 14 days	N/A	55.65	29.78	10.946	0.027	9.03	2.325	2.704
M15	Marine	Untreated	3.67	55.53	28.00	17.561	0.029	8.52	2.475	2.747
		60 °C, 18 MPa, 10 days	N/A	57.69	24.69	8.421	0.026	11.59	2.331	2.645
M16	Marine	Untreated	1.96	38.24	9.86	8.539	0.016	9.30	2.427	2.745
		60 °C, 18 MPa, 10 days	N/A	40.21	10.06	4.236	0.014	10.96	2.254	2.655
M17	Marine	Untreated	3.66	34.00	29.60	17.85	0.0245	6.62	2.708	2.775
		338K, 10 MPa, 15 days	N/A	38.50	28.40	15.25	0.0252	7.50	2.697	2.776
		338K, 15 MPa, 15 days	N/A	40.00	27.80	13.96	0.0267	7.92	2.67	2.726
		338K, 20 MPa, 15 days	N/A	40.20	26.00	9.640	0.0285	8.92	2.555	2.678
		308K, 15 MPa, 15 days	N/A	40.30	26.90	12.060	0.0275	8.09	2.562	2.691
		323K, 15 MPa, 15 days	N/A	41.30	27.20	12.200	0.0268	7.96	2.661	2.735
		338K, 15 MPa, 15 days	N/A	40.00	27.80	13.960	0.0267	7.92	2.67	2.726
		353K, 15 MPa, 15 days	N/A	39.70	27.00	13.430	0.0262	7.77	2.65	2.725
L17	lacustrine	Untreated	2.67	23.26	47.49	8.834	0.038	N/A	2.241	2.649
		80 °C, 15 MPa, 10 days	N/A	20.87	49.01	7.008	0.027	N/A	2.253	2.639
		80 °C, 15 MPa, 20 days	N/A	21.06	46.73	9.520	0.033	N/A	2.290	2.652
		80 °C, 15 MPa, 30 days	N/A	24.26	47.39	13.602	0.045	N/A	2.294	2.669
L18	lacustrine	Untreated	5.64	23.61	47.35	9.234	0.026	8.43	2.074	2.708
		30 °C, 5 MPa, 14 days	N/A	26.44	45.37	8.556	0.024	8.51	2.142	2.705
		80 °C, 20 MPa, 14 days	N/A	22.73	50.22	10.303	0.028	8.75	2.128	2.709
L19	lacustrine	Untreated	4.32	26.63	34.32	6.688	0.024	10.07	2.074	2.640
		30 °C, 5 MPa, 14 days	N/A	27.27	45.06	5.315	0.019	11.36	2.129	2.604
		80 °C, 20 MPa, 14 days	N/A	24.26	46.61	7.836	0.026	9.75	2.145	2.652
L20	lacustrine	Untreated	5.81	15.64	48.20	5.589	0.024	12.58	2.127	2.565
		60 °C, 18 MPa, 10 days	N/A	19.04	52.17	6.930	0.020	10.10	2.160	2.643

N/A=No Data.

decreased, and the average pore size is increased in marine shale samples. Conversely, the pattern of change in pore structure parameters of the lacustrine shales samples is less obvious, but with the TSSA and  $R_{ave}$  increasing after treatment. In general, the adsorption capacity of shale is dominated by SSA. It can be inferred from Table 2 that the adsorption capacity of marine shale decreases, and that of lacustrine shales increases, after ScCO<sub>2</sub> exposure. The pore structure of marine shales is more significantly affected by ScCO<sub>2</sub> than that of lacustrine shales (Pan et al., 2018a,b; Zhou et al., 2018a).

Several factors influence variation in pore structure parameters after ScCO<sub>2</sub> treatment. The results of the previous studies

are summarized as follows: (1) Marine shales are rich in quartz, calcite and feldspar and primarily develop intergranular and organic matter pores; lacustrine shales have a higher clay mineral content and largely develop intergranular and intragranular pores (Cheng et al., 2020; Rezaee et al., 2017; Yin et al., 2016). The differences in mineral composition and formation process of marine and lacustrine shales cause the differences in pore structure; (2) Carbonic acid generated in the dissolution of ScCO<sub>2</sub> in water can dissolve porous minerals, especially in clay-rich shales where the adsorption capacity and TPV are significantly decreased. (3) Adsorption-induced swelling narrows the pores, leading to a reduction of macro- and mesopore volume, while extraction and

dissolution mechanisms associated with ScCO<sub>2</sub> in organic matter and minerals reduce the number of smaller pores (Lu et al., 2021; Yin et al., 2016). After ScCO<sub>2</sub> treatment, the clay minerals in clay-rich shales tend to swell, narrowing the pores and converting the macropores into mesopores and potentially to micropores. In contrast to clay-rich shales, the dissolution of ScCO<sub>2</sub> results in a general increase of pore volume in quartz-rich shales (Huang et al., 2019). (4) Dissolution has a limited effect on pore structure, and the swelling effect induced by extraction and adsorption is the main controlling factor affecting the change of pore structure (Fatah et al., 2022a). (5) The surface potential energy of the shale changes due to the adsorption of CO<sub>2</sub>. The change in the potential energy of the surface is equal to the change in the potential energy of elasticity according to the principle of conservation of energy; this phenomenon causes the shale matrix to expand or contract depending on the mineral composition. In addition, the extent to which ScCO<sub>2</sub> affects the shale pore structure is highly dependent on shale heterogeneity.

### 3.2.4. Fractal dimension

Characterization by fractal dimension has been widely used to quantitatively describe pore surface roughness and the pore structure of heterogeneous porous media (Avnir and Jaroniec, 1989; Cheng et al., 2020; Zheng et al., 2018). Since the CO<sub>2</sub> adsorption isotherm is only related to pores smaller than 1 nm, the nitrogen adsorption isotherm is generally used to estimate the fractal dimension (D) – typically in the range between 2 and 3. The closer the value of D approaching 2 indicates the smoother the pore surface and the simpler the structure, with D approaching 3 representing a rougher pore surface and a more complex pore structure (Pfeifer and Avnir, 1983). By the N<sub>2</sub> adsorption data, the fractal dimension is estimated by applying the Frenkel–Halsey–Hill (FHH) model of Eq. (1) (Avnir and Jaroniec, 1989).

$$\ln V = (D - 3) \ln (\ln P_0/P) + C \quad (1)$$

where V is the adsorbed volume of N<sub>2</sub> at equilibrium vapor pressure (cm<sup>3</sup>), and P<sub>0</sub> and P are the saturated vapor and equilibrium pressures of the gas (MPa), respectively. C is a constant, and D is the fractal dimension of the heterogeneous porous media.

According to previous studies (e.g., Cheng et al., 2020; Huang et al., 2019; Hui et al., 2019; Jiang et al., 2016; Yang et al., 2022a), the adsorption/desorption isotherm hysteresis loops for N<sub>2</sub> mostly close at a relative pressure (P/P<sub>0</sub>) of ~0.42. The N<sub>2</sub> is mainly adsorbed on the shale surface at low relative pressures (0~0.45) and inside the pores at higher relative pressures (0.45~1.0). Accordingly, the fractal dimension D1 (P/P<sub>0</sub>:0~0.45) and D2 (P/P<sub>0</sub>:0.45~1.0) are used to characterize the roughness of the pore surface and the complexity of the pore structure, respectively.

#### (1) Factors influencing fractal dimension

Multiple factors control the shale fractal dimension (Bai et al., 2021; Li et al., 2022; Sun et al., 2017). In this paper, we discuss the relationship between D and total organic carbon content (TOC), mineral composition (quartz, clay minerals) and pore structure (TSSA, TPV and R<sub>avg</sub>, etc.).

Fractal dimensions D1 and D2 are both positively correlated with TOC content in shale, with correlation coefficients (R<sup>2</sup>) of 0.574 and 0.512, respectively (Fig. 4a). The fractal dimension of both pore surface and pore structure increase with an increase in TOC content, primarily attributed to the large number of nanoscale pores created when hydrocarbons were expelled from the organic matter during the thermal maturation of shale – and typically resulting in a complex pore surface and structure (Fu et al., 2022; Li et al., 2022).

There is a positive correlation between the fractal dimensions (D1 and D2) and the quartz content, with correlation coefficients (R<sup>2</sup>) of 0.564 and 0.374, respectively (Fig. 4b). The strong resistance of quartz to compaction preserves the primary intergranular pores but with the brittle quartz susceptible to microfracturing by external pressure (Yang et al., 2015). The location of the contact between quartz and clay and other flexible minerals frequently forms grain edge joints, where the pore structure is generally more complex. Quartz in marine shales, typically biogenic, has a positive correlation with TOC, as biogenic quartz is derived from different tectonic organisms, thereby developing complex organic matter pores and contributing to a larger fractal dimension (Jiang et al., 2019). The fractal dimension of shale is negatively correlated with the clay mineral content, with correlation coefficients (R<sup>2</sup>) of 0.523 and 0.511, respectively (Fig. 4c).

Fig. 4d–f shows the correlation between D and the pore structure. D increases with increasing TSSA and TPV and decreases with increasing R<sub>avg</sub>. The correlation between D and TSSA is stronger (R<sup>2</sup> ≥ 0.83). Therefore, it is presumed that TSSA is the main factor affecting the value of D. Generally, the degree of macropore development affects TPV and R<sub>avg</sub>, and the degree of micropore development affects TSSA. Combined with the correlation between D and pore parameters in Fig. 4, the narrower the R<sub>avg</sub>, the more micropores and mesopores are contained within the shale. The micropores and mesopores provide a larger TSSA, which results in a rough pore surface, complex structure, and the value of D increased. Correlations with the fractal dimensions have specific geological importance, for example, to distinguish among the formation of organic pores during the expulsion of hydrocarbons from organic matter, inorganic pores formed during diagenesis and controls on mineral composition and compaction effects. Thus, trends in the adsorption, storage, and migration of gas in shale can be analyzed to some extent by studying fractal dimensions.

#### (2) Change in fractal dimension after ScCO<sub>2</sub> exposure

The impact of ScCO<sub>2</sub> treatment on fractal dimension has been broadly investigated (e.g., Cheng et al., 2020; Fatah et al., 2022; Liu, 2017; Pan et al., 2018a; Zhou et al., 2022a). The fractal dimension obtained from the data of Pan et al. (2018a) shows a certain degree of regularity with changes in the duration of ScCO<sub>2</sub> treatment. D<sub>1</sub> and D<sub>2</sub> of marine shales decreased as the treatment time increased (Fig. 5a). Conversely, because the differences in mineral composition and pore structure between marine and lacustrine shales, D<sub>1</sub> of lacustrine shales increased as the treatment time increased, and D<sub>2</sub> first decreased and then increased as the treatment time increased (Fig. 5b). By extracting the data of Yang et al. (2022a) to calculate the value of D, the results show that D<sub>1</sub> and D<sub>2</sub> of the marine shales decreased with increasing pressure and D<sub>1</sub> and D<sub>2</sub> first increased and then decreased as temperature increased (Fig. 5c, d). Pan et al. (2018b) also investigated the variation in shale pore structure under Subcritical CO<sub>2</sub> (SubCO<sub>2</sub>, T = 30 °C and P = 5 MPa) and ScCO<sub>2</sub> (T = 80 °C and P = 20 MPa) treatment conditions (Fig. 5e, f). The decreasing trends in D are similar, but the effect of ScCO<sub>2</sub> treatment on shale pores is significantly greater than that of SubCO<sub>2</sub>, primarily due to the stronger dissolution and expansion effects associated with the ScCO<sub>2</sub> extraction mechanism. Overall, D<sub>2</sub> is generally larger than D<sub>1</sub>, which indicates that the pore structure is more complex than the pore surfaces. In addition, the fractal dimension of lacustrine shales is typically smaller than that of marine shale – indicating that the pore system is more complex in marine shales. The fractal dimension varies with ScCO<sub>2</sub> treatment conditions, resulting primarily due to the effect of temperature and pressure on the properties of ScCO<sub>2</sub> – which in turn affects the dissolution and expansion effects of ScCO<sub>2</sub> in shale and ultimately changes the complexity of the pore structure.

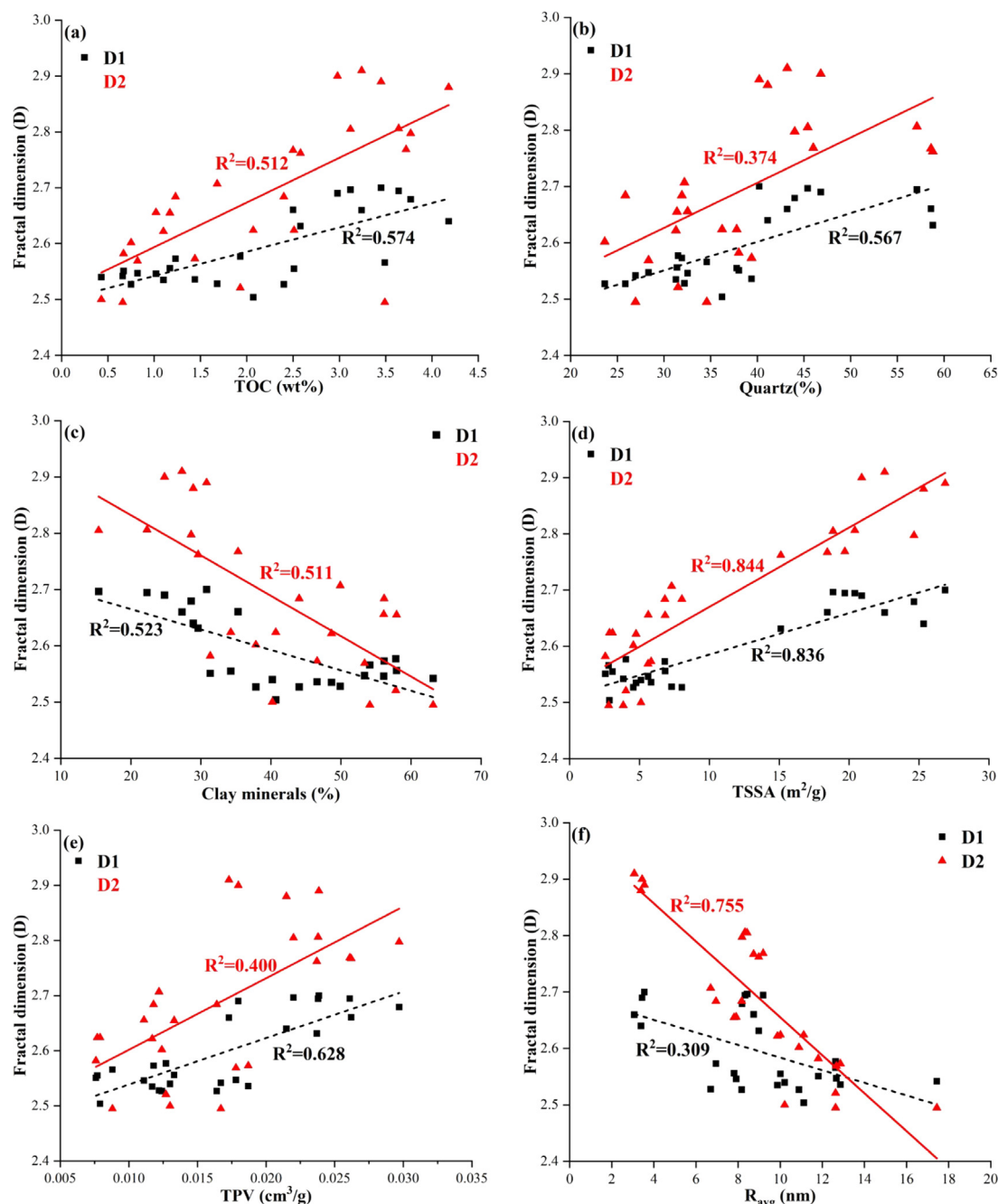


**Fig. 4.** Correlation of fractal dimension  $D$  with total organic carbon (TOC), quartz content, clay mineral content, total specific surface area (TSSA), total specific surface area (TPV), and average pore size ( $R_{avg}$ ): (a) Fractal dimensions D1 and D2 have a significant positive correlation with TOC content; (b) Fractal dimensions D1 and D2 both increase with an increase in quartz content; (c) Clay mineral content is negatively correlated with the fractal dimension; (d) TSSA is the major factor affecting the fractal dimension and shows a positive correlation with the fractal dimension; (e) TPV is an important factor influencing the fractal dimension, which has a significant positive correlation with the fractal dimension; (f) Negative/inverse correlation of fractal dimension  $D$  with  $R_{avg}$ .

Fig. 6 shows the correlation among shale pore structure, mineral composition, and fractal dimension  $D$  for different temperatures (a, b), pressures (c, d) and treatment times (e, f). The decreasing trends of D1 and D2 with increasing treatment temperature are not obvious (Fig. 6a, b); D1 and D2 of marine shales both decrease as the treatment pressure increases, and the trends with treatment temperature and pressure of D1 and D2 are similar to the overall trends of TSSA and clay mineral content (Fig. 6c, d). D1 and D2 of marine shales decreases with time, D1 of lacustrine shales increases with time, with D2 generally decreasing over time followed by an increase — trends that are not obvious within changes related to pore structure and mineral composition

(Fig. 6e, f). This trend is intimately related mainly to the properties of  $\text{ScCO}_2$ . The solubility and pH of  $\text{CO}_2$  in aqueous solutions vary under different temperatures and pressures (Deng et al., 2018; Peng et al., 2013) — the solubility increasing as pressure increases and decreasing as temperature increases and the pH of the solution decreasing as pressure increases and increasing as temperature increases. When the  $\text{ScCO}_2$ -water solution solubility is elevated and the pH is depressed, the inorganic minerals will be more soluble and reactive to the fluids with a concomitantly greater effect on pore structure.

Fig. 7 shows the correlation between  $D$  and the pore structure parameters with  $\text{ScCO}_2$  treatment. Before treatment,  $D$  exhibited

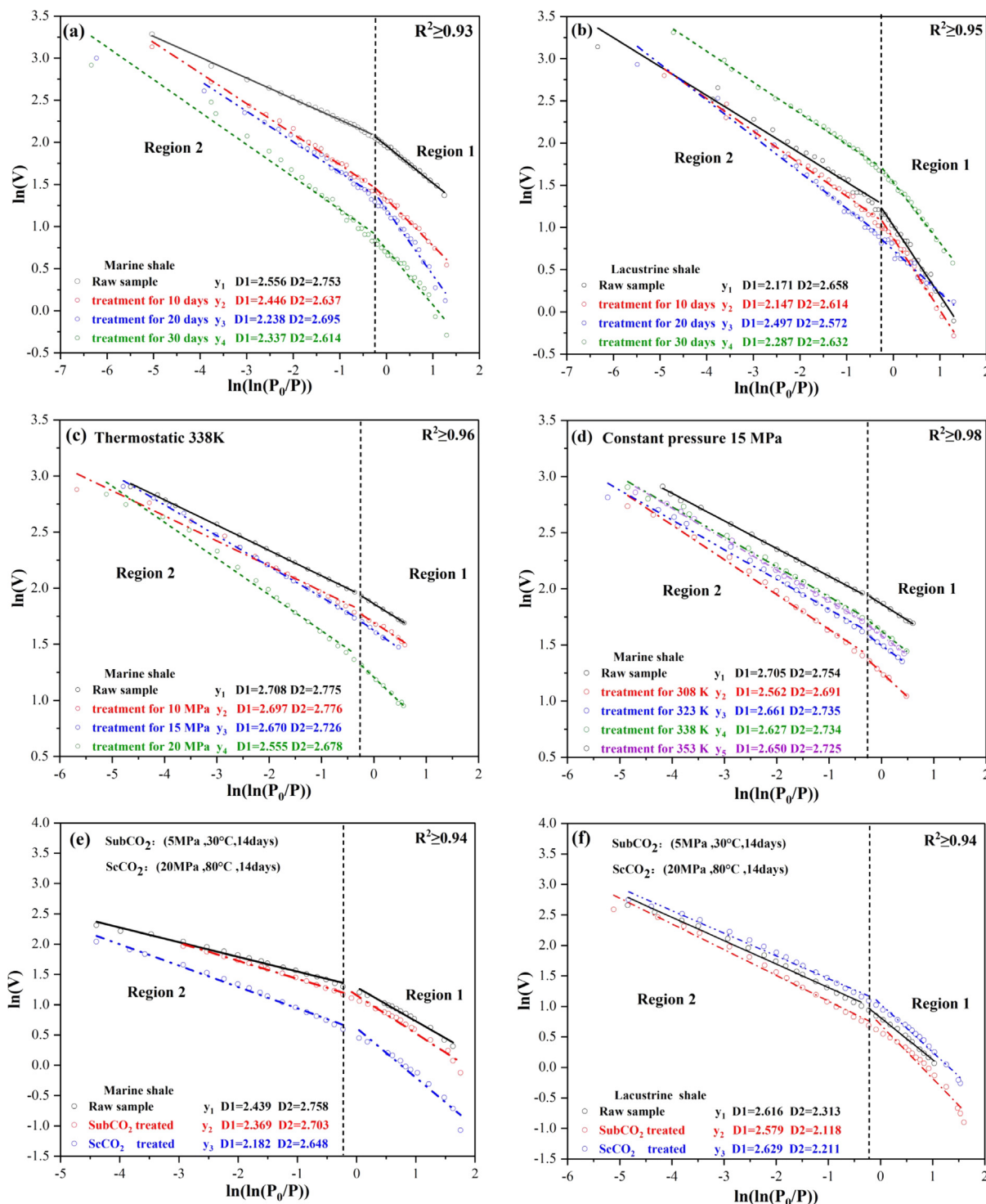


**Fig. 5.** Plots of  $\ln V$  vs  $\ln(\ln(P_0/P))$  from  $N_2$  adsorption data. Variation of: (a) Fractal dimension of marine shale with  $ScCO_2$  treatment time; (b) Fractal dimension of terrestrial shale with  $ScCO_2$  treatment time. (c) Effect of  $ScCO_2$  treatment pressure on the fractal dimension of marine shale at constant temperature; (d) Variation of fractal dimension of marine shale with  $ScCO_2$  treatment temperature at constant pressure; (e) Comparison of fractal dimensions after Subcritical  $CO_2$  (Sub $CO_2$ ) and  $ScCO_2$  treatment in marine shales; (f) Variation of fractal dimensions of terrestrial shales after Sub $CO_2$  and  $ScCO_2$  treatment.

a strong positive correlation with the TSSA ( $D1:R^2 = 0.833$ ,  $D2:R^2 = 0.667$ ) (Fig. 7a, b) and a weak negative correlation with the TPV ( $D1:R^2 = 0.216$ ,  $D2:R^2 = 0.211$ ) (Fig. 7c, d). After  $ScCO_2$  treatment, the correlation between  $D1$  and TSSA became weaker ( $R^2 = 0.446$ ) (Fig. 7a), the correlation between fractal dimension  $D2$  and TPV became stronger ( $R^2 = 0.469$ ) (Fig. 7d), while the correlation between  $D2$  and TSSA and the correlation between  $D1$  and TPV did not change significantly. This result is consistent

with the definition of  $D1$  and  $D2$  (Pfeifer and Avnir, 1983):  $D1$  is primarily controlled by TSSA, and TPV primarily controls  $D2$ . The results indicate that after the treatment with  $ScCO_2$ , the control of  $D1$  by TSSA is weakened, and  $D2$  by TPV is enhanced.

To date, the characterization of variations in the pore structure of shales as a result of interactions with  $ScCO_2$  remains sparse. However, pre-existing experimental data, combined with our new results, delineate clear differences between the response

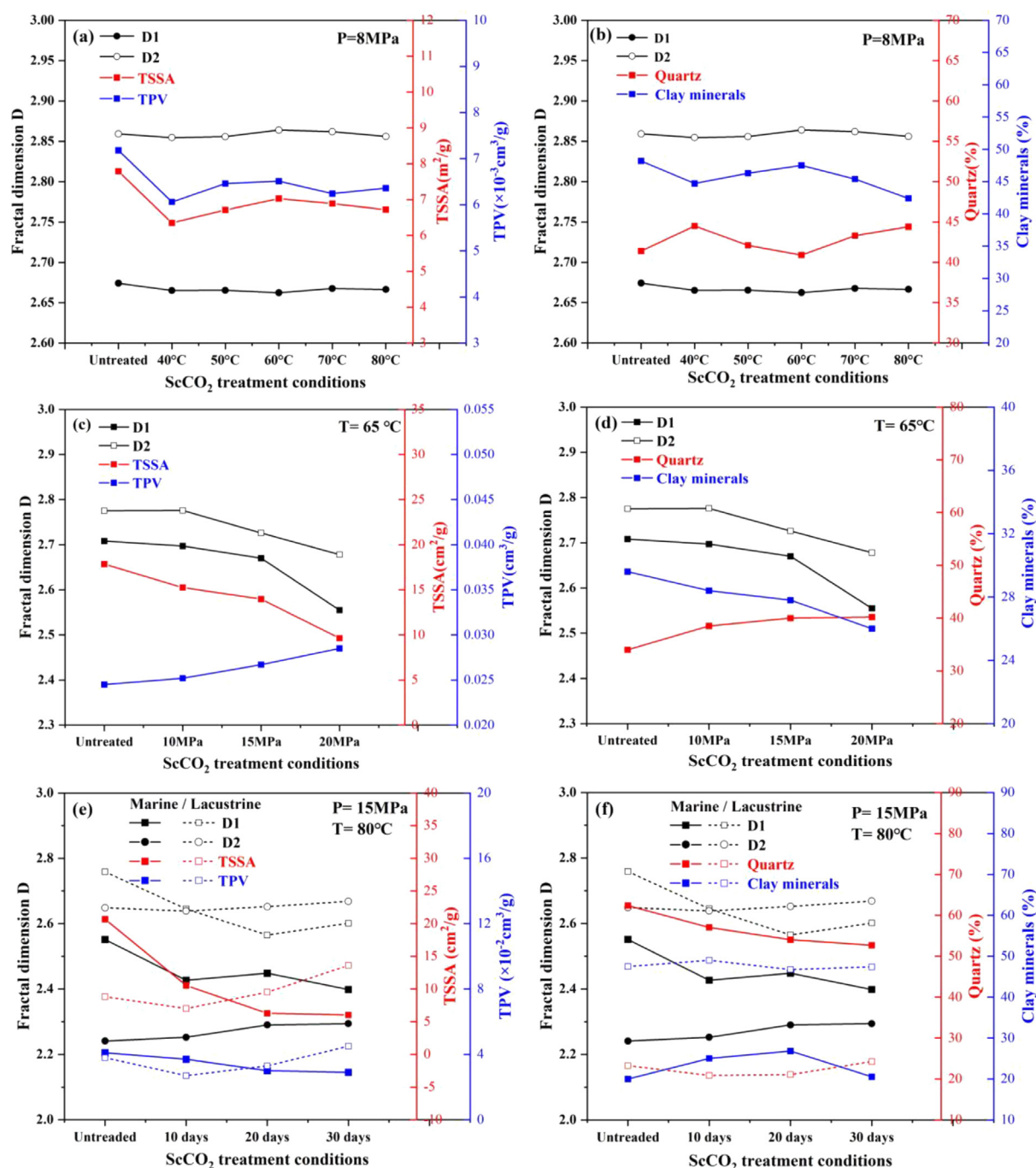


**Fig. 6.** Relationships between shale pore structure, mineral composition, and fractal dimension for different  $\text{ScCO}_2$  treatment conditions: (a, b) temperature; (c, d) pressure; and (e, f) time. The trends of D1 and D2 for marine shales are indistinct with increasing treatment temperature but decrease with increasing treatment pressure. D1 and D2 for marine shales decrease with time; D1 of lacustrine shale increases with time, and D2 first decreases and then increases with time.

of lacustrine and marine shales to  $\text{ScCO}_2$  treatment. Future studies should focus on lacustrine shales, where the data are limited, to investigate mechanisms and controls on the significant differences in evolution between lacustrine and marine shales exposed to  $\text{ScCO}_2$ .

#### 4. Changes in $\text{CO}_2$ and $\text{CH}_4$ adsorption capacity post- $\text{ScCO}_2$ treatment

##### 4.1. Single component adsorption of $\text{CO}_2$ and $\text{CH}_4$

Gas adsorption on shale surfaces is controlled by physical adsorption resulting from weak van der Waals forces prescribing the

electrostatic interplay between the adsorbate (gas molecules) and the adsorbent (shale) (Brunauer et al., 1940). The micropores enhance this interplay in the shale, which exhibits a wider internal surface area and confining conditions that force the fluid–solid phases closely enough for weak dipole–dipole interplays to occur and bind the gas to the shale surfaces (Nelson, 2009).

The gas adsorption capacity is the basis for characterizing reservoirs and predicting the volume of gas storage. There are significant differences in gas adsorption in different types of shales (viz., marine shale versus lacustrine shale). The adsorption volume in marine shales is generally greater than that in lacustrine shales (Fig. 8a, b). In addition, the adsorption volume of shale for different types of gases differs significantly – the adsorption

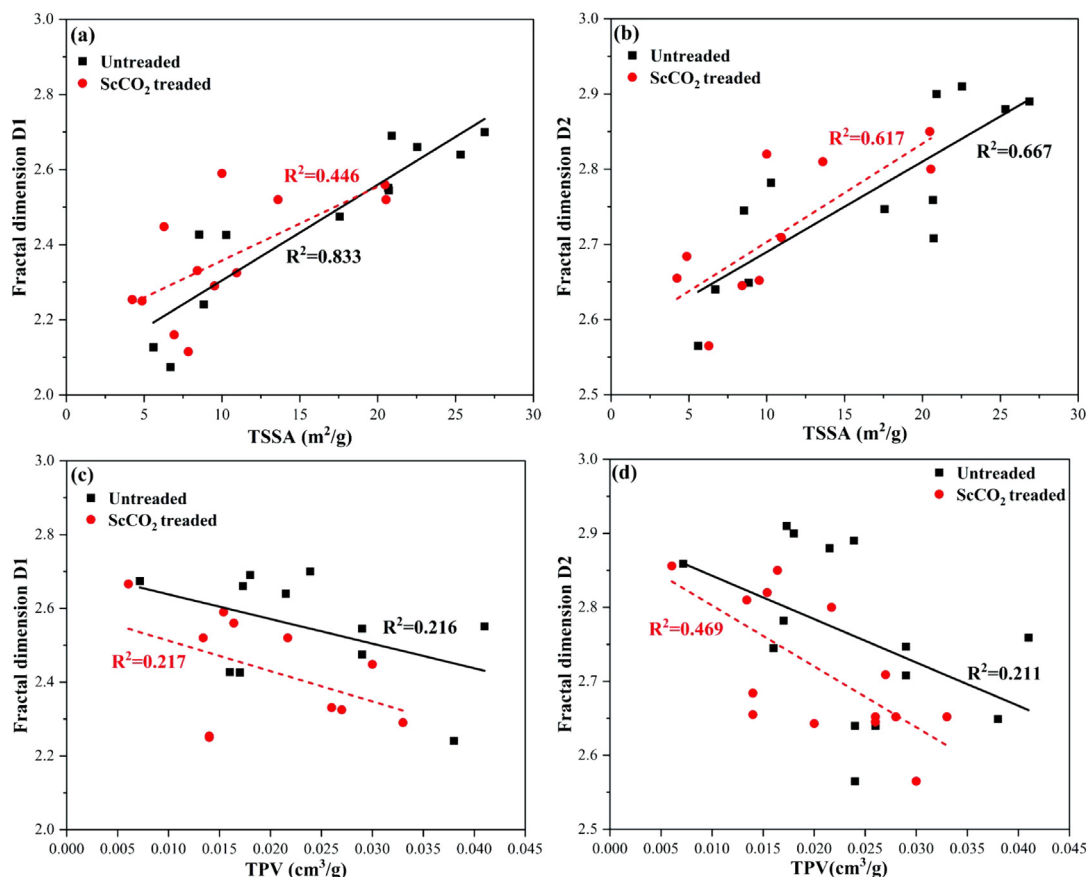


**Fig. 7.** Relationship between fractal dimension and pore structure both before and after  $\text{ScCO}_2$  treatment: (a, b) Fractal dimension versus total surface area; and (c, d) Fractal dimension versus total pore volume. Before treatment, the fractal dimension exhibited a strong positive correlation with the total specific surface area (TSSA) (D1:  $R^2 = 0.833$ , D2:  $R^2 = 0.667$ ) and a weak negative correlation with the total pore volume (TPV) (D1:  $R^2 = 0.216$ , D2:  $R^2 = 0.211$ ). After the  $\text{ScCO}_2$  treatment, the correlation between fractal dimension D1 and TSSA was weakened ( $R^2 = 0.446$ ), and the correlation between fractal dimension D2 and TPV strengthened ( $R^2 = 0.469$ ).

volume of shale for  $\text{CO}_2$  is larger than that for  $\text{CH}_4$ , confirming the feasibility of injecting  $\text{CO}_2$  to enhance the extraction of shale gas.

The absolute adsorption volume of  $\text{CH}_4$  on shale monotonically increases with increasing pressure and asymptotes to a constant at high pressure (Fig. 8a) (Li et al., 2017a; Weniger et al., 2010). The adsorption volume of  $\text{CO}_2$  also increases monotonically with pressure toward the supercritical transition point, with the adsorption curve of  $\text{CO}_2$  reaching a maximum at the pressure where the gas becomes supercritical. Any further increase in pressure leads to the monotonic desorption of  $\text{CO}_2$ , which is related to the phase change of  $\text{CO}_2$  around the supercritical state (Strubinger et al., 1991; Weniger et al., 2010). The density of  $\text{CO}_2$  increases as the state changes from gaseous to a supercritical fluid, and this change facilitates the overall  $\text{CO}_2$ -shale interplay by binding energy and more molecular layers attached to the shale surface (Schaefer et al., 2014b). With the continuous adsorption of  $\text{CO}_2$ , the curve gradually reaches a peak (as LMX3, WF4, YC curve in Fig. 8b), the pressure keeps increasing to bind the gas molecules more closely together, and the stabilization energy of the  $\text{ScCO}_2$  molecules increases. Meanwhile, the adsorptive energy of the adsorbate-adsorbent decreases, resulting in the dominance of desorption as the main mechanism. The resulting decrease in the adsorption curve can be observed in the isotherm (Fig. 8b). It is worth noting that the paper only describes single-component adsorption of  $\text{CO}_2$  and  $\text{CH}_4$  under simulated shale reservoir conditions. When  $\text{CO}_2$  and  $\text{CH}_4$  binary gases are injected in different ratios, more complex phenomena of concurrent  $\text{CO}_2$  and  $\text{CH}_4$  adsorption will occur (Busch et al., 2003).

#### 4.2. Changes in $\text{CH}_4$ and $\text{CO}_2$ adsorption parameters

Shale is a microporous adsorbent. The Langmuir adsorption model is based on the adsorption of a monomolecular layer and is representative of the adsorption of gas molecules on solid surfaces at low pressure (Langmuir, 1916, 1918). The Langmuir model is:

$$V_p = V_L P / (P_L + P) \quad (2)$$

where  $V_p$  is the adsorption volume ( $\text{cm}^3/\text{g}$ );  $P$  is the equilibrium pressure (MPa);  $V_L$  is the Langmuir volume ( $\text{cm}^3/\text{g}$ ), also known as the limiting adsorption volume, which refers to the maximum adsorption volume per gram of adsorbent surface covered with a full monomolecular layer;  $P_L$  refers to the Langmuir pressure (MPa), corresponding to the pressure at which the adsorption volume reaches half of  $V_L$ . Some scholars believe that the BET model (considering multilayer adsorption) and the Ono-Kondo model are more satisfactory choices (Bai et al., 2021; Duan et al., 2016; Rani et al., 2019; Sakurovs et al., 2007). Whether adsorption in shale can be described through a single model remains a point of debate. Several widely used adsorption models were presented, applied, and compared by Tang et al. (2017) and Yin et al. (2016) to reveal the characteristics and preferred applications of these adsorption models. In addition, the desorption of  $\text{CH}_4$  in shale is much easier than before  $\text{ScCO}_2$  treatment as the  $V_L$  of  $\text{CH}_4$  decreases and  $P_L$  increases with the  $\text{ScCO}_2$ -shale interplay – which is beneficial in improving shale gas recovery. However, the decrease in  $V_L$  and increase in  $P_L$  of  $\text{CO}_2$  can be detrimental

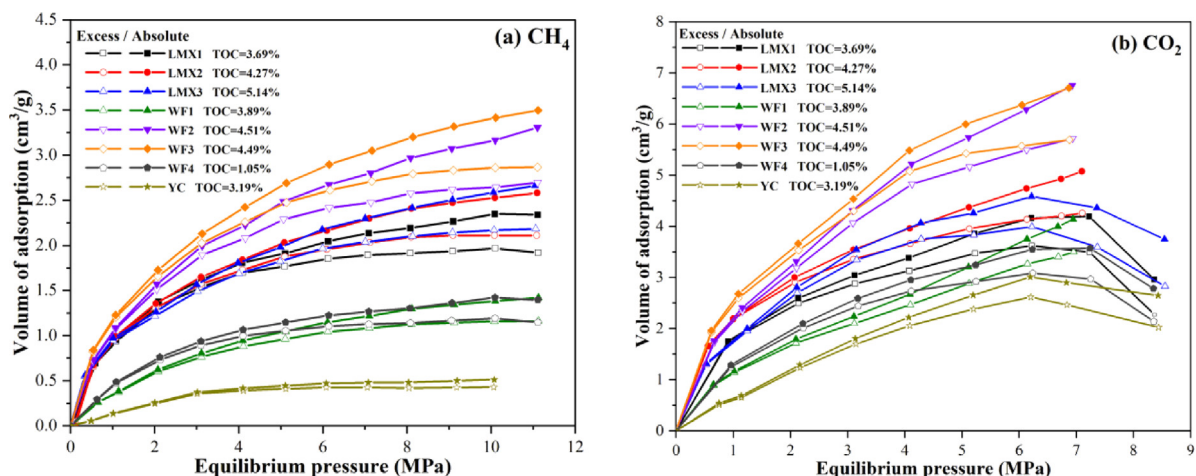


**Fig. 8.** Isotherms for  $\text{CH}_4$  (a) and  $\text{CO}_2$  (b) adsorption on shale samples at 45 °C (Data from (Liu, 2017)). The adsorption volume of  $\text{CO}_2$  is significantly greater than that of  $\text{CH}_4$  in shale. With an increase in equilibrium pressure, the volume of  $\text{CH}_4$  adsorption increases monotonically and gradually asymptotes to equilibrium; the volume of  $\text{CO}_2$  adsorption increases with an increase in equilibrium pressure before decreasing below as threshold pressure ( $P \approx 7.4$  MPa) (e.g. LMX3, WF4 and YC in Fig. 8b).

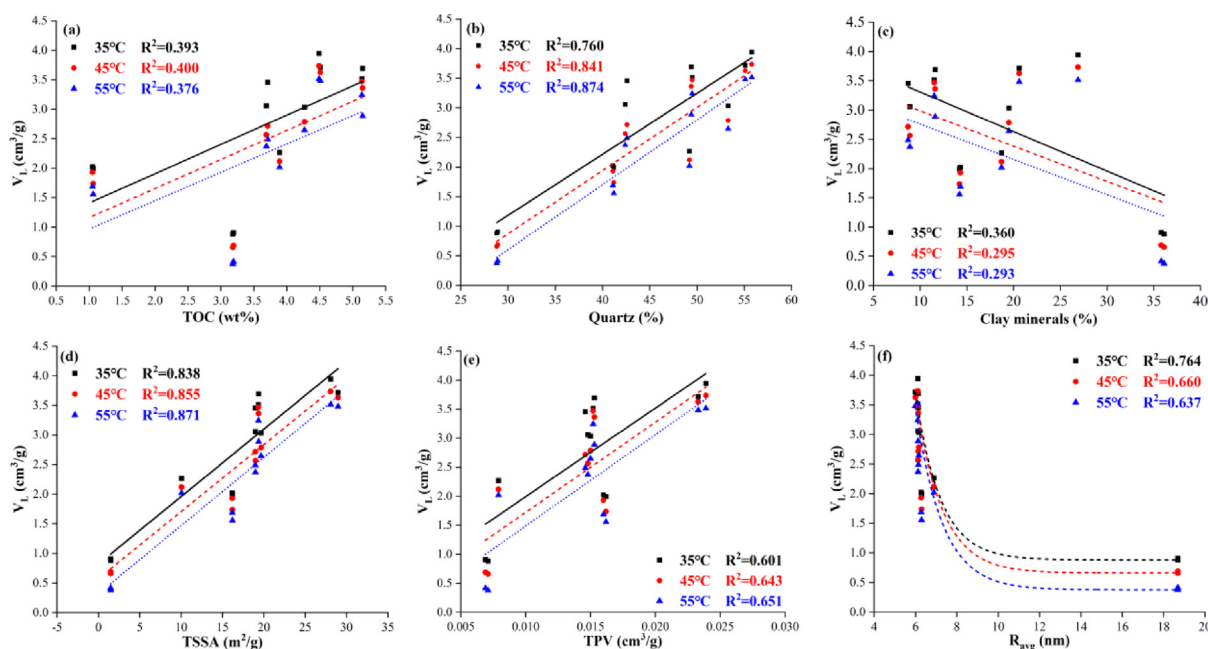


**Fig. 9.** Correlation of Langmuir volume ( $V_L$ ) of  $\text{CH}_4$  with total organic carbon (TOC), mineral composition and pore parameters at 45 °C: (a) TOC; (b) Quartz; (c) Clay minerals; (d) Total specific surface area (TSSA); (e) Total pore volume (TPV); and (f) Average pore size ( $R_{\text{avg}}$ ). The  $V_L$  of  $\text{CH}_4$  is positively correlated with TOC, quartz content, TSSA and negatively correlated with clay minerals and  $R_{\text{avg}}$ .  $V_L$  decreases with increasing temperature.

to the storage of  $\text{CO}_2$ , which may cause a reduction in the ultimate storage capacity of  $\text{CO}_2$  in shale gas reservoirs (Zhou et al., 2019a, 2022b). The optimal temperature and pressure conditions maximizing gas recovery and  $\text{CO}_2$  storage may vary due to the significant effect of interplay temperature and pressure effects on  $V_L$  and  $P_L$ .

#### 4.2.1. $\text{CO}_2$ and $\text{CH}_4$ adsorption capacity before $\text{ScCO}_2$ treatment

Figs. 9 and 10 illustrate the correlation between the Langmuir volume ( $V_{L-\text{CH}_4}$  and  $V_{L-\text{CO}_2}$ ) and TOC (Figs. 9a, 10a), mineral composition (Figs. 9b–c, 10b–c), and pore structure (Figs. 9d–f, 10d–f). Correlations of  $V_{L-\text{CO}_2}$  were found to be generally poorly correlated with various influencing factors compared to  $V_{L-\text{CH}_4}$ . The primary reason is that  $\text{CH}_4$  is predominantly physisorbed on shale, while there is also a relatively weak chemisorption between  $\text{CO}_2$  and shale in addition to physical adsorption (Bernard

et al., 2010). Thus, the influence of shale pore structure is more dominant for  $\text{CO}_2$  adsorption than  $\text{CH}_4$ . Therefore, the relationship between  $V_{L-\text{CH}_4}$  and TOC, mineral composition and pore parameters will be mainly discussed in this paper.  $V_{L-\text{CH}_4}$  shows strong positive correlations with TOC, quartz content, TSSA and TPV but negative correlations with clay minerals and  $R_{\text{avg}}$ . The correlation between  $V_{L-\text{CO}_2}$  and these factors is similar to that of  $V_{L-\text{CH}_4}$  but weaker. The adsorption volume of both  $\text{CH}_4$  and  $\text{CO}_2$  decreases with an increase in temperature (Figs. 9 and 10) – this is mainly because the physical adsorption of gas molecules on the shale surface is a spontaneous free-energy-reducing and exothermic process (Klewiah et al., 2020; Lu et al., 1995) and the amount of adsorption decreases with increasing temperature (Guo et al., 2017; Rexer et al., 2014).

The  $V_L$  of  $\text{CH}_4$  and  $\text{CO}_2$  are positively correlated with D1 and D2, with a stronger correlation for  $\text{CH}_4$  (Fig. 11a, b); the  $P_L$  of  $\text{CH}_4$

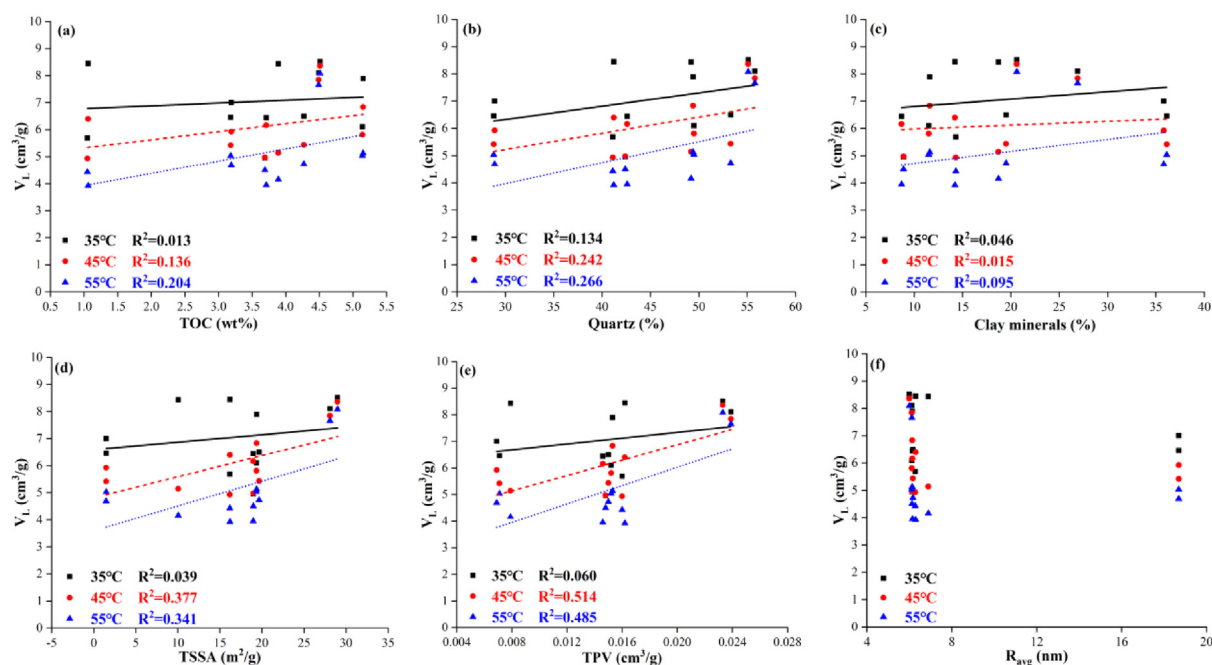


**Fig. 10.** Correlation of Langmuir volume ( $V_L$ ) of  $\text{CO}_2$  with total organic carbon (TOC), mineral composition, and pore parameters at 45 °C: (a) TOC; (b) Quartz; (c) Clay minerals; (d) Total specific surface area (TSSA); (e) Total pore volume (TPV); and (f) Average pore size ( $R_{\text{avg}}$ ). The  $V_L$  of  $\text{CO}_2$  is positively correlated with TOC, quartz content, TSSA and negatively correlated with clay minerals and  $R_{\text{avg}}$ . The correlation is overall similar to that of  $\text{CH}_4$  but weaker.  $V_L$  of  $\text{CH}_4$  also decreases with increasing temperature.

and  $\text{CO}_2$  are negatively correlated with D1 and D2, with a stronger correlation for  $\text{CO}_2$  (Fig. 11c, d). The strong correlation between D and  $V_L$  indicates that the relationship between shale heterogeneity and gas adsorption capacity is intimately related. Typically, the more developed shale micropores become, the larger the value of the fractal dimension, the more developed the shale micropores and the stronger their adsorption capacity. Therefore, D serves as an important index parameter to characterize the adsorption capacity of shale gas. A negative correlation between D and  $P_L$  indicates that the more heterogeneous the shale, the lower the pore pressure required to achieve the same adsorption volume, favorable to shale gas adsorption. Moreover, the negative correlation between D and  $P_L$  for  $\text{CO}_2$  is stronger, which means that the stronger the shale heterogeneity, the smaller the pressure required to reach a certain volume of  $\text{CO}_2$  adsorption in the shale. These characteristics are favorable to the geological storage of  $\text{CO}_2$  and the efficient extraction of  $\text{CH}_4$  from shale with  $\text{CO}_2$  (Lu et al., 2021; Mastalerz et al., 2009; Nuttall et al., 2009; Zhou et al., 2022b).

#### 4.2.2. $\text{CO}_2$ and $\text{CH}_4$ adsorption capacity after $\text{ScCO}_2$ treatment

After  $\text{ScCO}_2$  treatment, the shape of the  $\text{CH}_4$  adsorption isotherms of the samples is similar to that of the original samples, although the absolute adsorption volume of  $\text{CH}_4$  is significantly reduced (Fig. 12a). Likewise, the shape of  $\text{CO}_2$  adsorption isotherms also does not change significantly following  $\text{ScCO}_2$  treatment, and the absolute adsorption volume is significantly reduced post-treatment — consistent with the adsorption isotherm pattern of  $\text{CH}_4$  (Fig. 12b). This is consistent with the changes in SSA in the pore structure parameters as mentioned before. The SSA of shale, especially micropores, is reduced to different degrees after  $\text{ScCO}_2$  exposure, and micropores have an important influence on shale adsorption capacity (Bernard et al., 2010). Therefore, the variations in pore structure result in the reduction of  $V_L$  of  $\text{CO}_2$  and  $\text{CH}_4$ . The variation of  $V_L$  and  $P_L$  with  $\text{ScCO}_2$  treatment pressure (Fig. 13a, b) and temperature (Fig. 13d, e). From an overall perspective, the  $V_L$  of both  $\text{CH}_4$  and  $\text{CO}_2$  decrease

as the treatment temperature and pressure increase. Conversely,  $P_L$  for both  $\text{CH}_4$  and  $\text{CO}_2$  decrease as the treatment temperature increases and increase as the pressure decreases.

$V_L$  is calculated using the Langmuir equation and compared with the correlations of various factors. All correlations are observed to be stronger after treatment than before treatment, it implies that the  $\text{ScCO}_2$  treatment strengthens the connection between  $V_L$  and D, TSSA, and TPV (Fig. 14a–f). D and  $V_L$  are strongly and positively correlated (Fig. 14a, d), indicating that the complexity of the shale pore surface and structure dominates  $V_L$ . Combined with the previous analysis, the heterogeneity of the shale generally decreases after  $\text{ScCO}_2$  treatment, while the correlation between  $V_L$  and pore structure, and between  $V_L$  and D become stronger. Presumably, the reduction in shale heterogeneity promotes the connection between  $V_L$  and pore structure.

#### 4.3. Factors influencing shale adsorption capacity

Micropores appear as the primary factor affecting the adsorption capacity of shale, as smaller pores yield larger SSA and stronger adsorbent–adsorbent interplay energy compared to larger pores (Tang et al., 2017; Zhao and Wang, 2019; Zhou et al., 2022a). There are various factors affecting the shale adsorption capacity, which are mainly determined by two aspects: (1) shale properties, such as kerogen type, rock type, TOC, mineral composition, and pore structure, and (2) geological conditions and environments in which the shale gas is stored, such as temperature, pore pressure and moisture contents of the shale gas reservoirs.

##### 4.3.1. Influence of kerogen type

Kerogen is the fraction of organic matter (OM) in sedimentary rocks which remains insoluble in organic solvents (Ujiié, 1978). The kerogen is classified into three types (kerogen types I, II and III), and the classification depends primarily on the type of the source rock and the diagenetic environment (Boyer et al., 2006). By investigating the  $\text{CH}_4$  adsorption capacity of the Buckinghorse

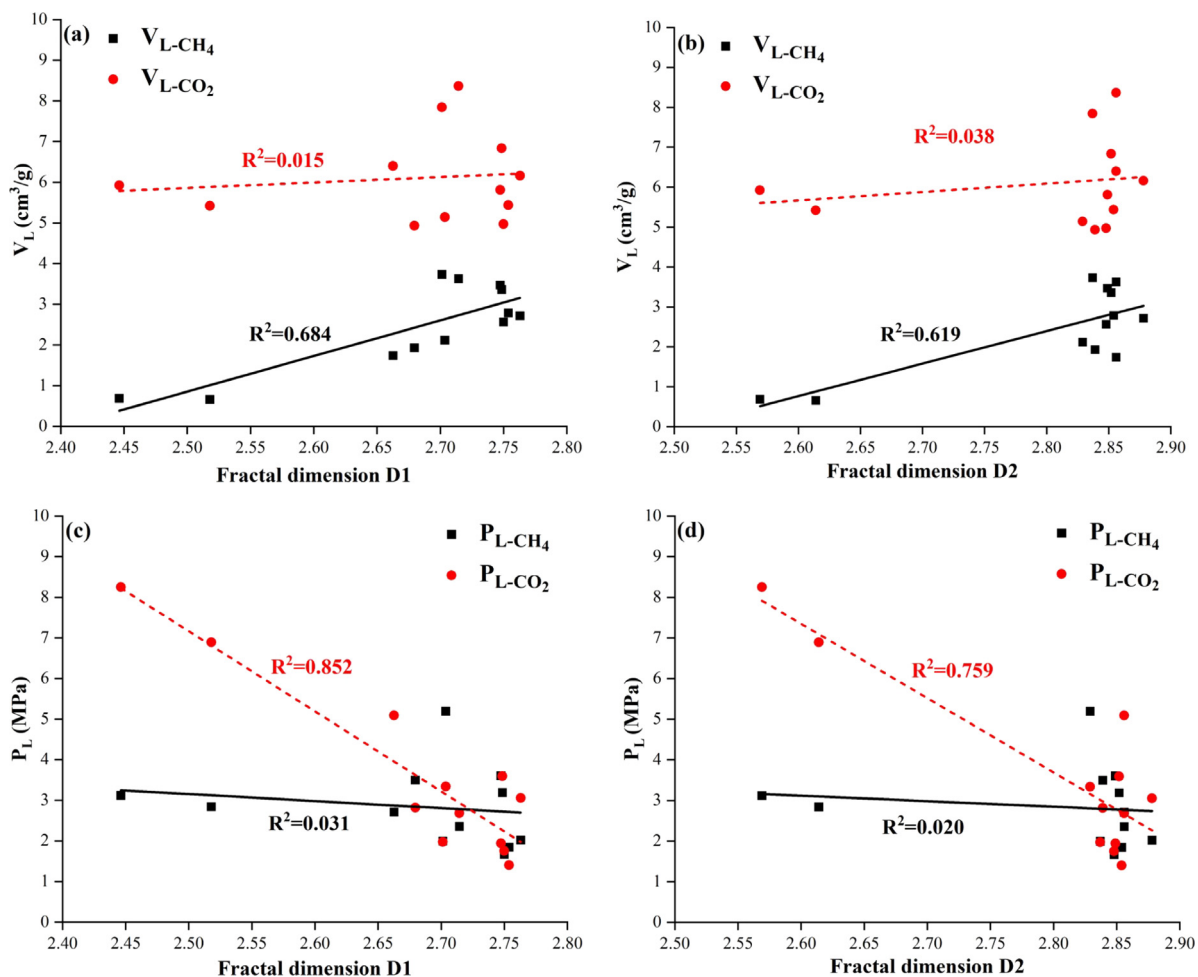


**Fig. 11.** The relationship between fractal dimension and Langmuir volume ( $V_L$ ) and Langmuir pressure ( $P_L$ ) at 45 °C. From: (a, b) The  $V_L$  of  $CH_4$  and  $CO_2$  are positively correlated with fractal dimensions D1 and D2, and the  $V_L$  of  $CH_4$  is more strongly correlated with the fractal dimensions D1 and D2; (c, d) The  $P_L$  of  $CH_4$  and  $CO_2$  are negatively correlated with the fractal dimension, and the  $P_L$  of  $CO_2$  is more strongly correlated with the fractal dimension (D1 and D2).

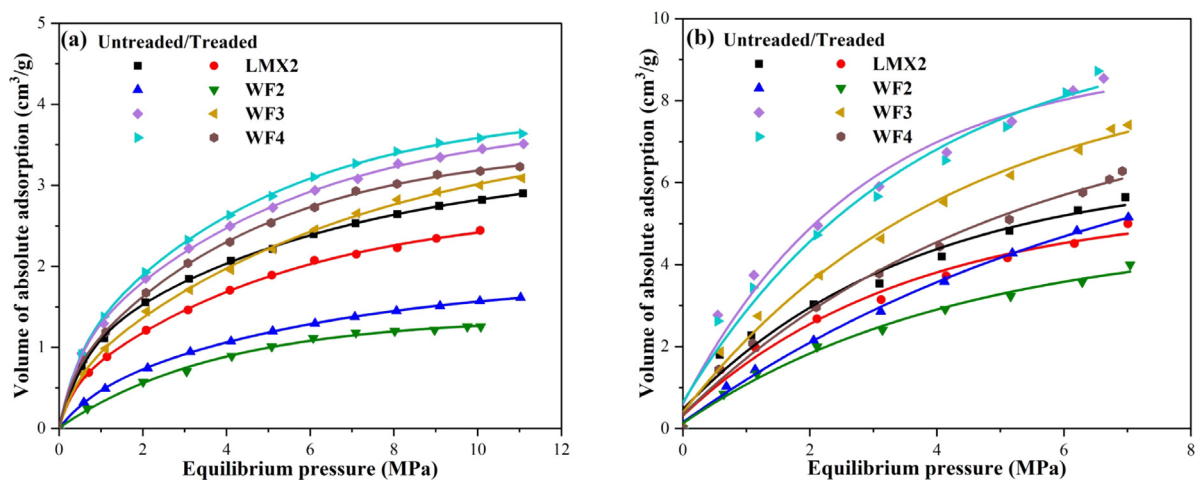


**Fig. 12.** Volume of absolute adsorption both before and then after  $ScCO_2$  treatment (a:  $CH_4$ ; b:  $CO_2$ ) (Data from (Liu, 2017)). The overall form of both  $CO_2$  and  $CH_4$  adsorption isotherms in the shale did not change significantly after the  $ScCO_2$  treatment, although the absolute adsorption volume of the shale decreased after treatment.

Formation in Canada, Chalmers and Bustin (2008) observed the capacity trend to be: Type II/III mixtures > Type III > Type II > Type I on a per unit TOC volume basis, and they argued that the more mature the kerogen, the more micropores and hydrocarbons are produced at a certain temperature. High-pressure (0–16 MPa)

methane adsorption experiments on organic-rich massive shale showed that the magnitude of  $CH_4$  adsorption volume was in the order of Type III > Type II > Type I at experimental temperature conditions of 35°, 50°, and 65 °C (Fig. 15a) (Zhang et al., 2012) and the adsorption volume decreased with increasing temperature.

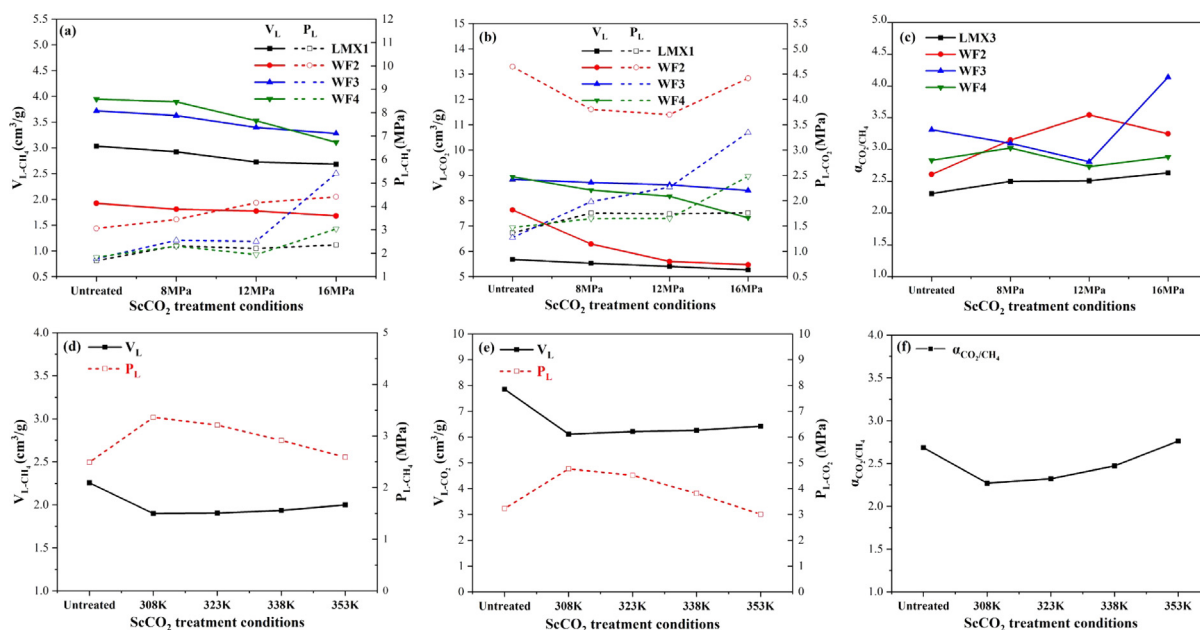


**Fig. 13.** Variation of Langmuir volume ( $V_L$ ), Langmuir pressure ( $P_L$ ) and selectivity factor  $\alpha_{CO_2/CH_4}$  with  $ScCO_2$  treatment pressure (a, b, c) and temperature (c, d, e). The  $V_L$  of both  $CH_4$  and  $CO_2$  decreased with increasing treatment pressure and increased with increasing temperature. Conversely, the  $P_L$  of both  $CH_4$  and  $CO_2$  increased with increasing treatment pressure and decreased with increasing temperature.  $\alpha_{CO_2/CH_4}$  increased with increasing  $ScCO_2$  treatment pressure and temperature.

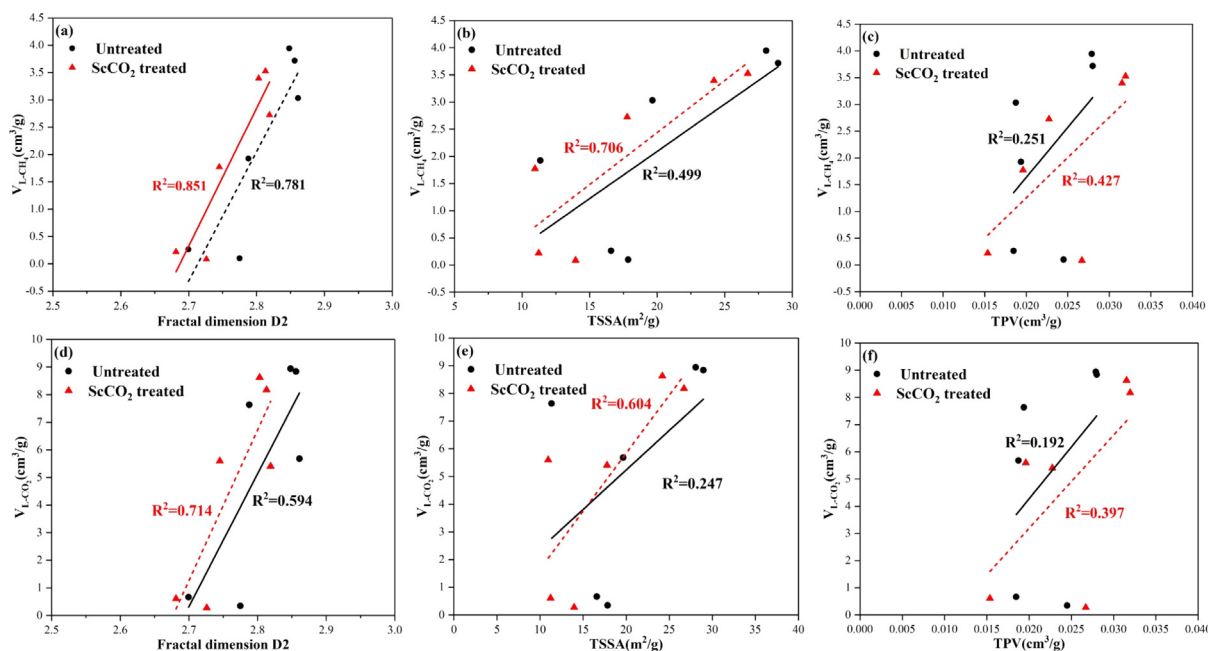


**Fig. 14.** Relationship between Langmuir volume ( $V_L$ ) versus fractal dimension D for: (a, d), total specific surface area (TSSA) (b, e) and total pore volume (TPV) (c, f) before and after  $ScCO_2$  treatment. The  $V_L$  of  $CH_4$  and  $CO_2$  are positively correlated with fractal dimension, TSSA, and TPV both before and after  $ScCO_2$  treatment. These correlations strengthen after treatment.

This is primarily due to the increase in the relative fraction of aromatic hydrocarbons represented from Type I to Type III compared to the aliphatic and naphthenic hydrocarbons (Helgeson et al., 2009; Welte and Tissot, 1984).

#### 4.3.2. Influence of TOC and mineral composition

The positive correlation between TOC content and  $V_L$  of  $CH_4$  is shown in Fig. 9a and has been reported by others (e.g., Cancino et al., 2017; Chang et al., 2017; Heller and Zoback, 2014; Krooss et al., 2002; Pozo et al., 2017; Rexer et al., 2014). A large number of micropores pervade organic matter providing greater

micropore SSA and micropore volume (Cao et al., 2015; Zhou et al., 2018b). Micropores are the major medium for natural gas adsorption; thus, shale with high TOC typically has a greater adsorption capacity (Gu et al., 2023). However, the correlation in our data for this paper remains weak (Fig. 9a), suggesting that the adsorption of  $CH_4$  on shale is influenced by a combination of factors, including TOC (Gasparik et al., 2014; Zou et al., 2017).

The quartz content is strongly and positively correlated with  $V_L$  partly due to the increase in TOC content in the shale as quartz content increases (Tao et al., 2019). In addition, the brittleness of quartz results in the susceptibility to microfractures when

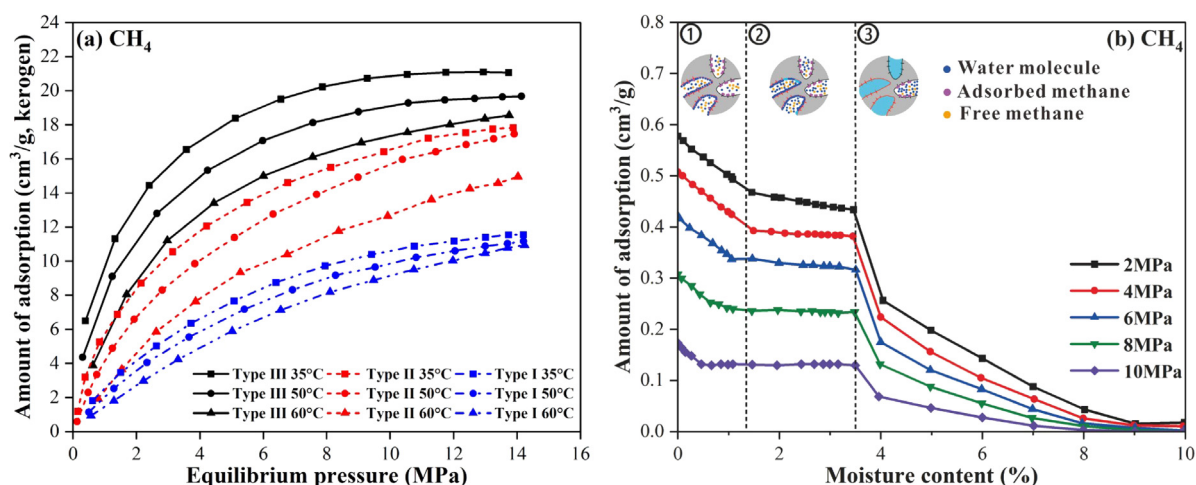


**Fig. 15.** Factors affecting the volume of CH<sub>4</sub> adsorption with (a) Temperature, Kerogen, and (b) moisture (Modified from Fan et al. (2018), Zhang et al. (2012)). Adsorption capacity trend: kerogen Type II/III mixtures > Type III > Type II > Type I on a per unit total organic carbon (TOC) volume basis. Adsorption volume decreases with increasing temperature but decreases with increasing moisture content and divides among three main stages of decline.

subjected to external pressure, which, in turn, provides more SSA for the adsorption of methane in the shale (Zhou et al., 2022a). However, a poor negative correlation between the  $V_L$  of CH<sub>4</sub> and clay mineral content is shown in Fig. 9c due to the complex clay mineral type and the stronger heterogeneity. Chen et al. (2016), Du et al. (2021) and Han et al. (2017) found that the multi-scale pores developed by clay minerals can provide storage space for CH<sub>4</sub> even though different types of clay minerals have widely varying adsorption capacities. By studying the adsorption capacity of pure clay minerals, Ji et al. (2012) found that the Langmuir volume of different clay minerals follows the order: montmorillonite > illite > chlorite at the same pressure. Therefore, the combination of different types of clay minerals in shale affects the gas adsorption capacity of shale. The experimental data selected in this paper only considered the effect of the total clay mineral content on the adsorption capacity and did not strictly distinguish between different types of clay minerals. This ultimately led to an insignificant correlation between the adsorption capacity of shale and the total clay mineral content.

#### 4.3.3. Influence of pore structure

TSSA and TPV both exhibit strong positive linear correlations with  $V_L$ . Physical adsorption is the main adsorption mechanism for gas in shale (Yang et al., 2015). Therefore the larger TSSA of the shale, the more sites the shale provides for gas adsorption, which is ultimately favorable for shale gas adsorption (Bernard et al., 2010). Lacustrine shales generally contain larger pores, and marine shales have more mesopores and micropores (Pan et al., 2018a). Regarding the correlation between  $R_{avg}$  and  $V_L$ , the overall correlation is negative.  $R_{avg}$  is strongly influenced by the macropores; therefore, the correlation between  $R_{avg}$  and adsorption capacity is poor. In addition, the gas in shale is primarily stored in the micropores – thus, future investigations should focus on the effect of micropores on the adsorption capacity.

#### 4.3.4. Influence of temperature

One of the key factors affecting the state of shale gas deposits is temperature. As shown in Figs. 9 and 15a, the volume of shale adsorption decreases with increasing temperature, consistent with the conclusions reached by other researchers (e.g., Guo et al., 2017; Rexer et al., 2014). According to the available literature, it is known that the physical adsorption of gas molecules on the shale surface occurs as a spontaneous free-energy-reducing and exothermic process, and the volume of adsorption decreases

with increasing temperature (Klewiah et al., 2020; Lu et al., 1995; Meray and Sinayuc, 2018). All the above indicate that the lower the temperature, the more favorable the gas adsorption in the shale.

#### 4.3.5. Influence of moisture

A negative correlation links moisture content and methane adsorption capacity (Fan et al., 2018). The relation between methane adsorption water content is divided into three stages with two intervening thresholds (Fig. 15b) (Fan et al., 2018): (1) linearly decreasing; (2) marginally decreasing; and (3) convex decreasing stage. The major mechanisms leading to this result can be summarized as follows. For the first stage of shale with low moisture content, water is adsorbed on the clay pore surface as a monolayer (Hatch et al., 2012), with pore surfaces of clay and organic matter providing the major adsorption sites of methane. Methane is primarily adsorbed on the pore surfaces of clay minerals and organic matter. As the moisture content increases, the methane adsorption sites are occupied by monolayer water molecules, resulting in a linear decrease in methane adsorption capacity (Day et al., 2008; Ren et al., 2017). The first threshold is reached after the hydrophilic surface in the shale is completely occupied by a monolayer of water with multilayer adsorption of water molecules occurring on the clay mineral surface when the water content exceeds the first threshold. In the second stage, the decrease in methane adsorption is negligible with increasing moisture uptake; the methane adsorption curve shows a convex decrease above the second threshold, which indicates that water in the organic pores condenses and the surface area for methane adsorption decreases due to water blockage (Fan et al., 2018; Mattia et al., 2012).

#### 4.4. Changes in adsorption selectivity factor

The selectivity factor for the sorption of CO<sub>2</sub> over CH<sub>4</sub> ( $\alpha_{CO_2/CH_4}$ ) is widely used to characterize the competing adsorption behavior of CO<sub>2</sub> and CH<sub>4</sub> in shale. This parameter reflects the ability of CO<sub>2</sub> to displace CH<sub>4</sub> and then store CO<sub>2</sub> (Duan et al., 2016).  $\alpha_{CO_2/CH_4}$  is estimated by Eq. (3):

$$\alpha_{CO_2/CH_4} = (x_{CO_2}/y_{CH_4})/(x_{CH_4}/y_{CO_2}) \\ = (V_{L-CO_2}/P_{L-CO_2})/(V_{L-CH_4}/P_{L-CH_4}) \quad (3)$$

where  $x$  is the molar fraction of a specific gas in the adsorptive phase. The variable  $y$  is the molar fraction of a specific gas in the

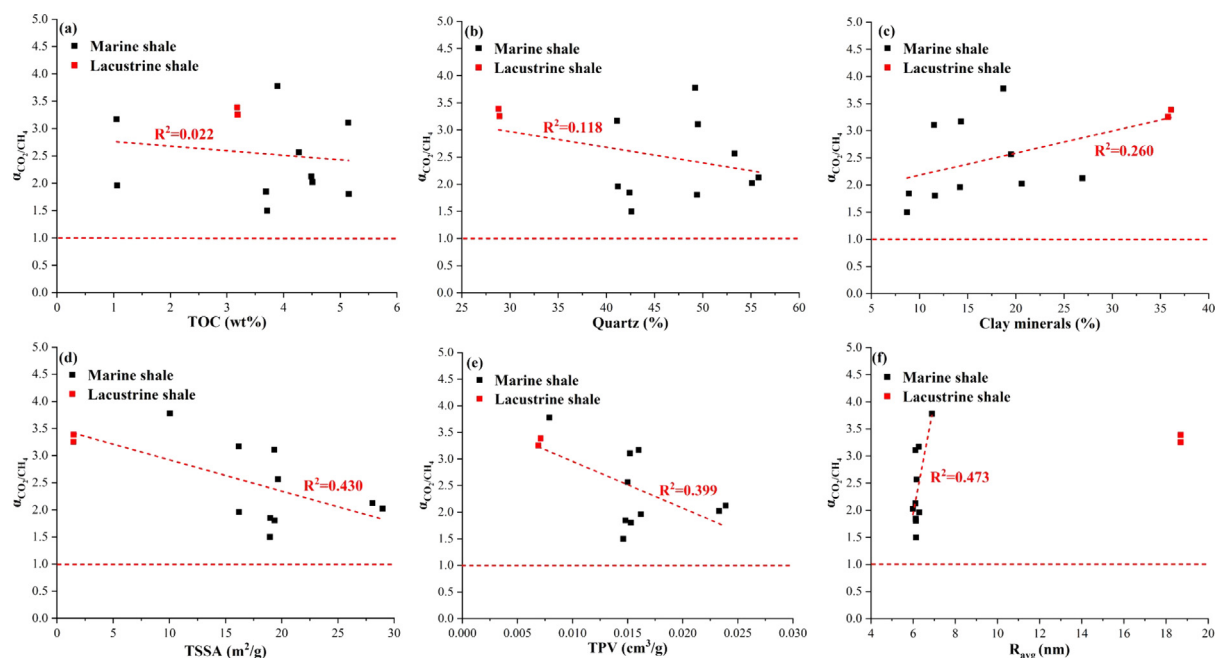


**Fig. 16.** Correlation of shale selectivity factors ( $\alpha_{\text{CO}_2/\text{CH}_4}$ ) with (a) Total organic carbon (TOC), (b, c) mineral composition, and (d, e, f) pore structure.  $\alpha_{\text{CO}_2/\text{CH}_4}$  is negatively correlated with TOC ( $R^2 = 0.022$ ), quartz content ( $R^2 = 0.118$ ), total specific surface area (TSSA) ( $R^2 = 0.430$ ), and total pore volume (TPV) ( $R^2 = 0.399$ ) and positively correlated with clay minerals ( $R^2 = 0.260$ ) and average pore size ( $R_{\text{avg}}$ ) ( $R^2 = 0.473$ ).

free gas phase. Variables  $V_L$  and  $P_L$  are the Langmuir volume and pressure of the types of gas, respectively, where  $V_L$  and  $P_L$  are the same as in Eq. (2).

An extensive literature (e.g., Cancino et al., 2017; Duan et al., 2016; Pusch et al., 2012; Yang et al., 2022a) shows that the temperature and pressure conditions and the TOC, Ro, pore structure and mineral composition of the shale affect the selectivity for  $\text{CO}_2$  and  $\text{CH}_4$  adsorption. In addition, the selectivity factor  $\alpha_{\text{CO}_2/\text{CH}_4}$  calculated by the Langmuir equation is always greater than 1, which identifies that the shale preferentially adsorbs  $\text{CO}_2$  from a mixture of  $\text{CO}_2$  and  $\text{CH}_4$ , and therefore guarantees the feasibility of  $\text{CO}_2$  replacing  $\text{CH}_4$  (Lu et al., 2021). As shown in Fig. 16a–f,  $\alpha_{\text{CO}_2/\text{CH}_4}$  is negatively correlated with TOC ( $R^2 = 0.022$ ), quartz content ( $R^2 = 0.118$ ), TSSA ( $R^2 = 0.430$ ) and TPV ( $R^2 = 0.399$ ), and positively correlated with clay mineral content ( $R^2 = 0.260$ ) and  $R_{\text{avg}}$  ( $R^2 = 0.473$ ). For  $R_{\text{avg}}$ , due to the excessive difference between the marine and lacustrine shales and the limited amount of lacustrine data, only the correlation with the marine shale is analyzed in this paper. The results of the analysis show that the correlations between  $\alpha_{\text{CO}_2/\text{CH}_4}$  and the factors involved in Fig. 16 are all poor. Compared with TOC and mineral composition factors, the pore structure factors correlate better with  $\alpha_{\text{CO}_2/\text{CH}_4}$ , indicating that pore structure is the dominant factor affecting adsorption capacity, while TOC and mineral composition mainly affect adsorption capacity indirectly by influencing pore structure. In addition, since  $\alpha_{\text{CO}_2/\text{CH}_4}$  is determined by  $V_L$  and  $P_L$  for  $\text{CO}_2$  and  $\text{CH}_4$  adsorption in shale, each variable has its own influencing factors, which lead to the final calculated  $\alpha_{\text{CO}_2/\text{CH}_4}$  being jointly controlled by multiple factors and weakly correlated with single factors.

As shown in Fig. 16, both D1 and D2 are negatively correlated with the selection factor  $\alpha_{\text{CO}_2/\text{CH}_4}$ . As the fractal dimension increases,  $\alpha_{\text{CO}_2/\text{CH}_4}$  decreases but is always greater than 1. The correlation between D2 and  $\alpha_{\text{CO}_2/\text{CH}_4}$  fits better relative to that for D1 and  $\alpha_{\text{CO}_2/\text{CH}_4}$  – rate of decrease of the curve starts to increase when D1 reaches about 2.65 (Fig. 17a) and the rate of decrease of the curve increases when D2 reaches about 2.8 (Fig. 17b). In summary, it is speculated that there is a sudden shift in the

correlation between  $\alpha_{\text{CO}_2/\text{CH}_4}$  and the fractal dimension. When D1 reaches about 2.65, and D2 reaches about 2.8, the heterogeneity of the shale is stronger. However,  $\alpha_{\text{CO}_2/\text{CH}_4}$  starts to decline rapidly, indicating that the heterogeneity is not conducive to  $\text{CO}_2$ -ESGR above a certain threshold of heterogeneity. In addition,  $\alpha_{\text{CO}_2/\text{CH}_4}$  shows an increasing trend with an increase in the  $\text{ScCO}_2$  treatment pressure and temperature (Fig. 13c, f). Therefore, in further investigations related to  $\text{CO}_2$ -ESGR, it is important to focus on the role of shale heterogeneity in influencing behavior and to determine a degree of shale heterogeneity that is conducive to the conduct  $\text{CO}_2$ -ESGR studies. Also, the influence of the treatment temperature and pressure of  $\text{ScCO}_2$  cannot be neglected.

## 5. Mechanisms of $\text{ScCO}_2$ -shale interactions

### 5.1. Mechanisms controlling pore structure variation

Natural gas is stored in shale reservoirs primarily in the free and adsorbed state. Compared with conventional natural gas reservoirs, shale reservoirs have complex pore systems with micron to nanometer-scale pores dominating (Bernard et al., 2010; Hao et al., 2013). TOC, thermal maturity, and inorganic mineral composition within the shale greatly affect the pore structure, which will directly affect shale gas transport and storage (Cancino et al., 2017; Lutyński et al., 2017; Wang et al., 2012).

Pore blockage in nanopores may become important after  $\text{ScCO}_2$  treatment (Huang et al., 2019). Such a pore-blocking phenomenon may be the result of the combined effect of physisorption, associative chemisorption and dissociative chemisorption in shale matrix (Huang et al., 2019). Fig. 18a1 illustrates the mechanisms and impacts of these three adsorption methods after  $\text{ScCO}_2$  treatment. Physisorption: after  $\text{ScCO}_2$  treatment, the adsorption sites for hydrocarbons in the shale are occupied by  $\text{CO}_2$  that gradually diffuses into the organic matter, causing part of the shale to swell and the nanopores to be blocked (Fig. 18a2) (Bernard et al., 2010; Pan et al., 2018a). Associative chemisorption:  $\text{ScCO}_2$  and water react chemically with part of the minerals in the shale to create new minerals, which may plug the nanopores

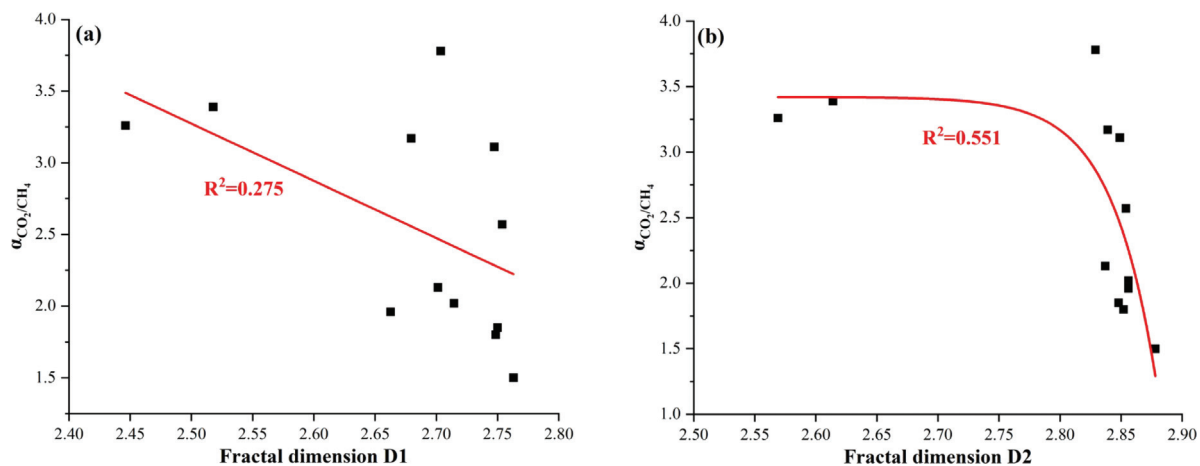


Fig. 17. Relationship between fractal dimension and selection factor ( $\alpha_{CO_2/CH_4}$ ) at 45 °C: (a) D1 is negatively correlated with  $\alpha_{CO_2/CH_4}$ ,  $R^2 = 0.275$ ; (b) D2 is negatively correlated with selection factor  $\alpha_{CO_2/CH_4}$ ,  $R^2 = 0.551$ ; and  $\alpha_{CO_2/CH_4}$  decreases rapidly for D1 > 2.65 and D2 > 2.80.

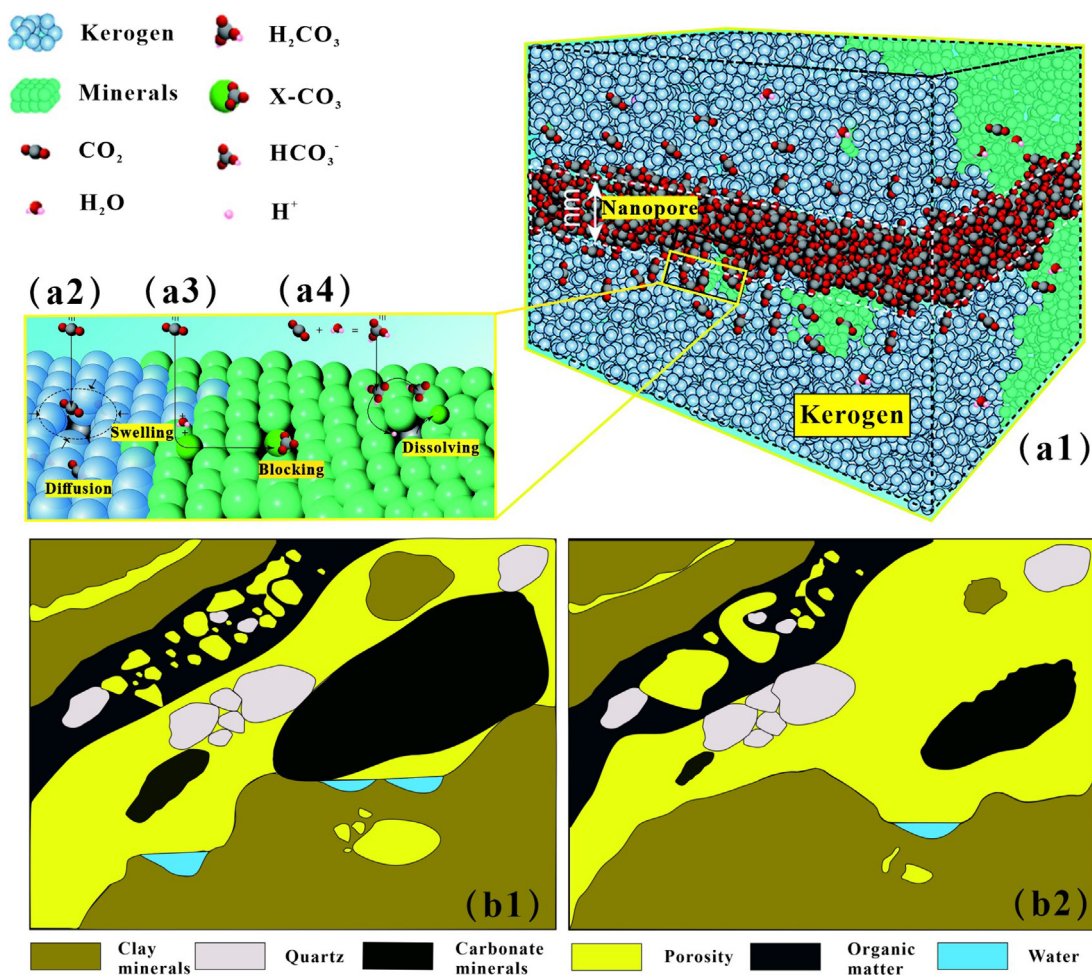


Fig. 18. Schematic depicting changes in pore structure driven by gas permeation (Fig. 18a1–a4 modified from Huang et al. (2019)). (a1) Nanopore comprising kerogen and minerals in a ScCO<sub>2</sub> environment. (a2) Physisorption; (a3) Associative chemisorption; (a4) Dissociative chemisorption; (b1) Schematic of pore structure before ScCO<sub>2</sub> treatment; then (b2) After ScCO<sub>2</sub> treatment where the pore structure of the shale undergoes a series of transformations, mainly influenced by the swelling effect caused by shale adsorption of ScCO<sub>2</sub> and the dissolution effect of ScCO<sub>2</sub> on shale minerals.

(Fig. 18a3) (Fatah et al., 2021). Dissociative chemisorption: after ScCO<sub>2</sub> is injected into the shale, CO<sub>2</sub> molecules combine with water molecules in the shale and then dissociate H<sup>+</sup> and HCO<sub>3</sub><sup>-</sup> on the surface, resulting in the dissolution of some minerals (carbonate minerals, clay minerals, etc.) and creating new nanopores

(Fig. 18a4) (Dai et al., 2020; Fatah et al., 2022; Kweon and Deo, 2017).

The mechanism of pore structure alteration under ScCO<sub>2</sub> has also been discussed in the published literature (Fatah et al., 2022a; Pan et al., 2018a; Yin et al., 2016). In summary, the

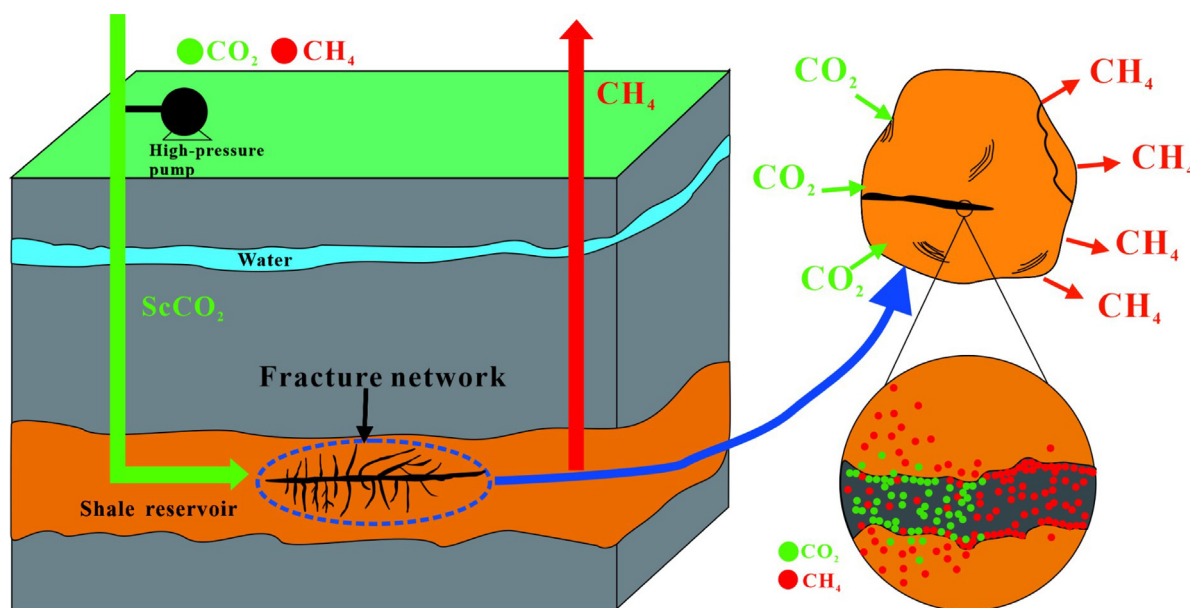


Fig. 19. Schematic depicting ScCO<sub>2</sub> replacement of native CH<sub>4</sub> where CO<sub>2</sub> molecules repel CH<sub>4</sub> molecules at different scales.

mechanisms of pore structure evolution can be summarized in two forms (Fig. 18b1, b2): (1) ScCO<sub>2</sub> has a strong dissolution and extraction capacity, which extracts some organic matter (aliphatic and aromatic hydrocarbons, etc.) and dissolves some inorganic minerals, resulting in larger pores or the generation of new nanopores (Fatah et al., 2022); (2) A portion of the minerals in shale (clay, etc.) swell after adsorption of CO<sub>2</sub>, resulting in the narrowing of pores and with the interplay of ScCO<sub>2</sub> with minerals in the shale matrix generate new materials, or the minerals precipitate and block the nanopores (Pan et al., 2018a). The mechanisms contributing to changes in the pore structure as a result of ScCO<sub>2</sub> exposure are intimately linked to the mineral composition as well as the original pore structure. The evolved pore structure after ScCO<sub>2</sub> treatment is largely influenced by the heterogeneity of the shale. Thus, future research should focus on the following: (1) Exploring the major composition of shale minerals as well as the original pore structure before exploring the variations of pore structure and other changes in shale after ScCO<sub>2</sub> treatment; (2) Comparing these two competing mechanisms and exploring which mechanism dominates changes in pore structure and morphology.

## 5.2. Mechanisms controlling competitive adsorption

CO<sub>2</sub> adsorption capacity to shale is greater than that for CH<sub>4</sub> (Billemont et al., 2013; Busch et al., 2003; Chareonsuppanimit et al., 2012). With the injection of ScCO<sub>2</sub> into shale gas reservoirs, CH<sub>4</sub> molecules will compete with CO<sub>2</sub> molecules for adsorption sites and thus will be displaced by CO<sub>2</sub>, enhancing the recovery of CH<sub>4</sub> as well as geological sequestering CO<sub>2</sub> (Fathi and Akkutlu, 2014; Lu et al., 2021). Fig. 19 illustrates this phenomenon of competing for adsorption between CO<sub>2</sub> and CH<sub>4</sub> molecules at different scales. CO<sub>2</sub> molecules replace CH<sub>4</sub> molecules by occupying the adsorption sites of the original CH<sub>4</sub> molecules, thus enhancing shale gas recovery. The mechanism of competitive shale gas adsorption and CO<sub>2</sub> replacement divides among the following points:

(1) The kinetic diameter of the CO<sub>2</sub> molecule is smaller than that of CH<sub>4</sub> (Cui et al., 2004; Li et al., 2009), allowing easier entry of the smaller diameter molecule to the pores. As a result, CO<sub>2</sub> molecules preferentially occupy adsorption sites in shale pores

over CH<sub>4</sub>, resulting in a higher probability of adsorption of the CO<sub>2</sub> molecule (Lan et al., 2019).

(2) The CH<sub>4</sub> molecule has a lower critical temperature than the CO<sub>2</sub> molecule. Since the physical adsorption process is an exothermic reaction, the lower the critical temperature, the more unfavorable the adsorption process. In shale, the heat of adsorption of CH<sub>4</sub> is reported to be less than that of CO<sub>2</sub>, with a greater heat of adsorption of gas indicating a greater affinity of the shale for that gas (Duan et al., 2016; Luo et al., 2015; Rexer et al., 2014). Conversely, the smaller the heat of adsorption of the gas, the easier it is to remove it by desorption in the shale (Lan et al., 2019).

(3) The diffusion coefficient of CH<sub>4</sub> is larger than that for CO<sub>2</sub> at the same temperature signaling rates of mass transfer at the same concentration gradient to be faster for CH<sub>4</sub> than for CO<sub>2</sub> (Pathak et al., 2018; Sui and Yao, 2016). Thus the mobility of CH<sub>4</sub> is stronger than that of CO<sub>2</sub>, which facilitates the replacement of CH<sub>4</sub> by CO<sub>2</sub> (Hu et al., 2017).

(4) The polarity of the CO<sub>2</sub> molecule is lower than that of CH<sub>4</sub>; thus the quadrupole moment and dipole moment of the CO<sub>2</sub> molecules are larger than those of CH<sub>4</sub> (Sui and Yao, 2016). Since physical adsorption is caused by van der Waals forces (Nelson, 2009), adsorbents with greater molecular polarity are more strongly favored for adsorption, implying that CO<sub>2</sub> is more easily adsorbed in shale.

## 6. Challenges and opportunities

Environmental protection has become a contemporary imperative, establishing CO<sub>2</sub> enhanced shale gas recovery and geological sequestration as a desirable mitigation strategy, albeit with various challenges and opportunities.

- (1) Currently, there is a paucity of data on lacustrine shales and controlled experiments on individual marine shales lack comparability. In addition, the vast majority of experiments are conducted on crushed shale samples, with experiments on intact samples challenging to conduct (Nuttal et al., 2005). Although the use of crushed samples is rapid and convenient, crushed samples do not accurately represent in-situ reservoir conditions as they alter the structure of the porous media (e.g., microfractures, etc.). Thus, future

studies should expand the data on lacustrine shales, systematically investigate the differences between marine and lacustrine shales in terms of microstructure and adsorption capacity and complete these on intact cores that represent real reservoir conditions.

- (2) Observations charting changes in composition following exposure to ScCO<sub>2</sub> are extensive. However, most experiments are limited to a single reaction between ScCO<sub>2</sub> and shale, there may be other substances such as deep brines and the reaction between ScCO<sub>2</sub> and shale under in-situ reservoir condition that influence reactions (Zheng et al., 2019). In addition, the time scale issue needs to be addressed to allow slow reactions to proceed to completion. Thus, future studies should combine numerical simulations, and consider the influence of brine on the reactions, to follow reactions under the influence of multiple factors on a longer time scale. Mechanisms of gas adsorption at high pressure and temperature require to be refined to further constrain shale gas adsorption mechanisms.
- (3) The adsorption experiments of single-component gas and CO<sub>2</sub>-CH<sub>4</sub> binary gases that have been performed to date are replete with differences in competing for adsorption behaviors (Du et al., 2022). Although the adsorption of mixtures of CO<sub>2</sub>-CH<sub>4</sub> will more closely replicate the response in reservoirs, there are fewer relevant mixed adsorption experiments, especially under the conditions of real reservoirs. In addition, the problem of quantifying mechanisms of dynamic exchange of CO<sub>2</sub>-CH<sub>4</sub> remains unsolved, including based on fundamental principles of thermodynamics (Liao et al., 2023). It is a promising approach as the heat of adsorption can accurately describe the physical and chemical properties of the adsorption process and the adsorption volume. In addition, the current study of the competitive adsorption of CH<sub>4</sub> and CO<sub>2</sub> is completed mainly under static conditions, which still differs from the gas exchange process in the actual shale reservoir situation. Fluid detection techniques (e.g., NMR) are promising methods to unobtrusively evaluate the dynamics of CH<sub>4</sub> and CO<sub>2</sub> in porous media (Zhao and Wang, 2019).

In summary, CO<sub>2</sub>-ESGR is a complex process that prompts significant changes in pore network structure and competitive adsorption as the central mechanisms in this interplay. Despite the complexity of the interplay mechanisms between ScCO<sub>2</sub> and shale, useful results are available at laboratory and field scales, and the relevant reactions in CO<sub>2</sub>-ESGR are gradually being investigated and clarified.

## 7. Conclusions

In order to systematically explore the pattern of alterations in shale that result from ScCO<sub>2</sub> treatment, experimental data on different types of shale (marine shales of the Longmaxi and Wufeng formations in the Sichuan basin and lacustrine shales of the Yanchang formation in the Ordos Basin and the Shahezi formation in the Songliao Basin) were compiled, synthesized, and analyzed. First, various test characterization methods (XRD, SEM and low-pressure gas adsorption technology) were used to evaluate the mineral composition and microstructure of different types of shale. Second, CH<sub>4</sub>/CO<sub>2</sub> adsorption experiments were used in the analysis of gas adsorption capacity. Subsequently, the shale was treated with ScCO<sub>2</sub>, and the changes in pore structure and gas adsorption capacity were analyzed both before and after treatment. On this basis, relationships between microstructure and adsorption capacity were established. Several main conclusions are drawn, as follows:

1. Several significant variations in microstructure are observed after ScCO<sub>2</sub> treatment. The interplay between ScCO<sub>2</sub> and the shales alters the mineral composition, which in turn affects the pore structure and adsorption capacity. Clay and carbonate mineral contents in both lacustrine and marine shales decreased significantly, and the relative content of quartz increased after ScCO<sub>2</sub> treatment. Mineralization reactions play a key role in the conduct of CO<sub>2</sub>-ESGR. As a result of the complexity of shale mineral composition, the mineralization reactions between ScCO<sub>2</sub> require further constraint. According to the low-pressure gas adsorption data following ScCO<sub>2</sub> treatment, the basic pore shapes within the shale did not alter dramatically, although TSSA, TPV, and the number of micropores decreased, and  $R_{avg}$  increased. Compared with lacustrine shales, the microstructure of marine shales is more significantly influenced by ScCO<sub>2</sub>.

2. Fractal dimensions D1 and D2 can quantitatively characterize the pore surface roughness and pore structure of heterogeneous porous media. D2 is invariably larger than D1, indicating that the pore structure is more complex than the pore surface. After ScCO<sub>2</sub> treatment, both D1 and D2 of the shale generally decreased, indicating that the pore surface and structure progressively transformed from complex to less complex. The apparent is that TSSA mainly controls D1, and TPV controls D2. The control of D1 by TSSA is weakened, and the control of D2 by TPV is strengthened after ScCO<sub>2</sub> treatment.

3. Various factors significantly influence the adsorption capacity of shale, including TOC, mineral composition, kerogen type, pore structure, moisture content, pressure, and temperature. The adsorption volume of CO<sub>2</sub> in shale is much larger than that of CH<sub>4</sub>, and the  $\alpha_{CO_2/CH_4}$  is consistently greater than 1, demonstrating the feasibility of CO<sub>2</sub> replacement of CH<sub>4</sub> in shale. The absolute adsorption volumes of both CH<sub>4</sub> and CO<sub>2</sub> decrease after ScCO<sub>2</sub> treatment, the  $V_{L-CH_4}$  and  $V_{L-CO_2}$  also decrease as the treatment temperature increases and as the treatment pressure decreases. These results since TSSA and TPV decrease as well as  $R_{avg}$  increases after ScCO<sub>2</sub> treatment, resulting in the observed variations in adsorption capacity. Changes in temperature and pressure affect the reaction between ScCO<sub>2</sub> and shale, mainly by affecting the properties of the ScCO<sub>2</sub>, in turn prompting changes in pore structure and adsorption capacity.

4. D1 and D2 are positively correlated with  $V_L$  and negatively correlated with  $P_L$  — indicating that stronger shale heterogeneity favors improved performance of CO<sub>2</sub> -ESGR. However, it is worth noting that both D1 and D2 are negatively correlated with  $\alpha_{CO_2/CH_4}$ . When the fractal dimension reaches a threshold (D1>2.65, D2>2.80),  $\alpha_{CO_2/CH_4}$  decreases rapidly, which is unfavorable for CO<sub>2</sub> displacement of CH<sub>4</sub> and sequestration of CO<sub>2</sub>.

5. Changes in shale microstructure driven by ScCO<sub>2</sub> exposure are mainly influenced by the swelling effect caused by the adsorption of ScCO<sub>2</sub> and the effect of the dissolution of minerals in shale. Mechanisms of competitive adsorption and ScCO<sub>2</sub> replacement for shale gas are controlled by molecular diameters, relative diffusion coefficients and polarity of the molecular components. The kinetic diameter of the CH<sub>4</sub> molecule is larger than that of CO<sub>2</sub>; the CH<sub>4</sub> molecule has a lower critical temperature than the CO<sub>2</sub> molecule; at the same temperature, the diffusion coefficient of CH<sub>4</sub> is larger than that of CO<sub>2</sub>, prompting a more rapid diffusion rate of CH<sub>4</sub> than CO<sub>2</sub>; and the polarity of CO<sub>2</sub> molecules is greater than that of CH<sub>4</sub> molecules. These factors contribute to the preferential sorption of CO<sub>2</sub> over CH<sub>4</sub> in shales, validating the feasibility of conducting CO<sub>2</sub>-ESGR.

## CRediT authorship contribution statement

**Shaoqiu Wang:** Data curation, Writing – original draft, Investigation. **Sandong Zhou:** Conceptualization, Formal analysis, Writing – review & editing, Supervision. **Zhejun Pan:** Writing – review & editing. **Derek Elsworth:** Writing – review & editing, Validation. **Detian Yan:** Project administration. **Hua Wang:** Supervision, Validation. **Dameng Liu:** Supervision. **Zhazha Hu:** Writing – review & editing.

## Declaration of competing interest

The authors declare that they have no known competing financial interests or personal relationships that could have appeared to influence the work reported in this paper.

## Data availability

Data will be made available on request.

## Acknowledgments

The project was supported by the National Natural Science Foundation of China (42102219, 42072204), the Open Funds for Hubei Key Laboratory of Marine Geological Resources, China University of Geosciences, PR China (MGR202104), the PetroChina Innovation Foundation, PR China (2020D-5007-0107), the Natural Science Foundation of Hubei Province, PR China (2019CFA028). And acknowledges support from the G. Albert Shoemaker endowment, PR China.

## References

- Alemu, B.L., Aagaard, P., Munz, I.A., Skurtveit, E., 2011. Caprock interaction with CO<sub>2</sub>: A laboratory study of reactivity of shale with supercritical CO<sub>2</sub> and brine. *Appl. Geochem.* 26 (12), 1975–1989. <http://dx.doi.org/10.1016/j.apgeochem.2011.06.028>.
- Ao, X., Lu, Y., Tang, J., Chen, Y., Li, H., 2017. Investigation on the physics structure and chemical properties of the shale treated by supercritical CO<sub>2</sub>. *J. CO<sub>2</sub> Util.* 20, 274–281. <http://dx.doi.org/10.1016/j.jcou.2017.05.028>.
- Avnir, D., Jaroniec, M., 1989. An isotherm equation for adsorption on fractal surfaces of heterogeneous porous materials. *Langmuir* 5 (6), 1431–1433. <http://dx.doi.org/10.1021/la00090a032>.
- Bai, B., Ni, H.-j., Shi, X., Guo, X., Ding, L., 2021. The experimental investigation of effect of supercritical CO<sub>2</sub> immersion on mechanical properties and pore structure of shale. *Energy* 228, 120663. <http://dx.doi.org/10.1016/j.energy.2021.120663>.
- Bernard, S., Horsfield, B., Schulz, H.-M., Schreiber, A., Wirth, R., Vu, T.T.A., Perssen, F., Könitzer, S., Volk, H., Sherwood, N., 2010. Multi-scale detection of organic and inorganic signatures provides insights into gas shale properties and evolution. *Geochemistry* 70, 119–133. <http://dx.doi.org/10.1016/j.chemer.2010.05.005>.
- Billemont, P., Coasne, B., De Weireld, G., 2013. Adsorption of carbon dioxide, methane, and their mixtures in porous carbons: effect of surface chemistry, water content, and pore disorder. *Langmuir* 29 (10), 3328–3338. <http://dx.doi.org/10.1021/la3048938>.
- Boyer, C., Kieschnick, J., Suarez-Rivera, R., Lewis, R.E., Waters, G., 2006. Producing gas from its source. *Oilfield Rev.* 18 (3), 36–49.
- Brunauer, S., Deming, L.S., Deming, W.E., Teller, E., 1940. On a theory of the van der Waals adsorption of gases. *J. Am. Chem. Soc.* 62 (7), 1723–1732.
- Busch, A., Krooss, B.M., Gensterblum, Y., Van Bergen, F., Pagnier, H., 2003. High-pressure adsorption of methane, carbon dioxide and their mixtures on coals with a special focus on the preferential sorption behaviour. *J. Geochem. Explor.* 78, 671–674. [http://dx.doi.org/10.1016/S0375-6742\(03\)00122-5](http://dx.doi.org/10.1016/S0375-6742(03)00122-5).
- Cancino, O.P.O., Pérez, D.P., Pozo, M., Bessieres, D., 2017. Adsorption of pure CO<sub>2</sub> and a CO<sub>2</sub>/CH<sub>4</sub> mixture on a black shale sample: Manometry and microcalorimetry measurements. *J. Pet. Sci. Eng.* 159, 307–313. <http://dx.doi.org/10.1016/j.petrol.2017.09.038>.
- Cao, T., Song, Z., Wang, S., Cao, X., Li, Y., Xia, J., 2015. Characterizing the pore structure in the Silurian and Permian shales of the Sichuan Basin, China. *Mar. Pet. Geol.* 61, 140–150. <http://dx.doi.org/10.1016/j.marpetgeo.2014.12.007>.
- Chalmers, G.R., Bustin, R.M., 2008. Lower cretaceous gas shales in northeastern British Columbia, Part I: geological controls on methane sorption capacity. *Bull. Can. Pet. Geol.* 56 (1), 1–21. <http://dx.doi.org/10.2113/gscpbull.56.1.1>.
- Chang, T., Shu, Y., Ma, Y., Xu, X., Niu, Y., 2017. Isothermal adsorption and desorption properties of marine shales on Longmaxi shale in South China. *Open J. Geol.* 7 (12), 1819. <http://dx.doi.org/10.4236/ojg.2017.712122>.
- Chareonsuppanimit, P., Mohammad, S.A., Robinson, Jr., R.L., Gasem, K.A., 2012. High-pressure adsorption of gases on shales: Measurements and modeling. *Int. J. Coal Geol.* 95, 34–46. <http://dx.doi.org/10.1016/j.coal.2012.02.005>.
- Chen, T., Feng, X.-T., Pan, Z., 2015. Experimental study of swelling of organic rich shale in methane. *Int. J. Coal Geol.* 150, 64–73. <http://dx.doi.org/10.1016/j.coal.2015.08.001>.
- Chen, S., Han, Y., Fu, C., Zhu, Y., Zuo, Z., 2016. Micro and nano-size pores of clay minerals in shale reservoirs: Implication for the accumulation of shale gas. *Sediment. Geol.* 342, 180–190. <http://dx.doi.org/10.1016/j.sedgeo.2016.06.022>.
- Cheng, Y., Zeng, M., Lu, Z., Du, X., Yin, H., Yang, L., 2020. Effects of supercritical CO<sub>2</sub> treatment temperatures on mineral composition, pore structure and functional groups of shale: Implications for CO<sub>2</sub> sequestration. *Sustainability* 12 (9), 3927. <http://dx.doi.org/10.3390/su12093927>.
- Cui, X., Bustin, R.M., Dipple, G., 2004. Selective transport of CO<sub>2</sub>, CH<sub>4</sub>, and n<sub>2</sub> in coals: insights from modeling of experimental gas adsorption data. *Fuel* 83 (3), 293–303. <http://dx.doi.org/10.1016/j.fuel.2003.09.001>.
- Curtis, J.B., 2002. Fractured shale-gas systems. *AAPG Bull.* 86 (11), 1921–1938.
- Dai, X., Wang, M., Wei, C., Zhang, J., Wang, X., Zou, M., 2020. Factors affecting shale microscopic pore structure variation during interaction with supercritical CO<sub>2</sub>. *J. CO<sub>2</sub> Util.* 38, 194–211. <http://dx.doi.org/10.1016/j.jcou.2020.01.021>.
- Daniel, R., Kaldi, J., 2012. Mercury-injection capillary-pressure analysis. In: *Atlas of Australian and New Zealand Hydrocarbon Seals: Worldwide Analogs for Cap Rocks and Intraformational Barriers in Clastic Depositional Settings*, Vol. 60.
- Das, D., Mishra, B., Gupta, N., 2021. Understanding the influence of petrographic parameters on strength of differently sized shale specimens using XRD and SEM. *Int. J. Mining Sci. Technol.* 31 (5), 953–961. <http://dx.doi.org/10.1016/j.ijmst.2021.07.004>.
- Day, S., Sakurovs, R., Weir, S., 2008. Supercritical gas sorption on moist coals. *Int. J. Coal Geol.* 74 (3–4), 203–214. <http://dx.doi.org/10.1016/j.coal.2008.01.003>.
- Deng, K., Lin, Y., Ning, H., Liu, W., Singh, A., Zhang, G., 2018. Influences of temperature and pressure on CO<sub>2</sub> solubility in saline solutions in simulated oil and gas well environments. *Appl. Geochem.* 99, 22–30. <http://dx.doi.org/10.1016/j.apgeochem.2018.10.013>.
- Du, X., Pang, D., Cheng, Y., Zhao, Y., Hou, Z., Liu, Z., Wu, T., Shu, C., 2021. Adsorption of CH<sub>4</sub>, n<sub>2</sub>, CO<sub>2</sub>, and their mixture on montmorillonite with implications for enhanced hydrocarbon extraction by gas injection. *Appl. Clay Sci.* 210, 106160. <http://dx.doi.org/10.1016/j.clay.2021.106160>.
- Du, X., Pang, D., Zhao, Y., Hou, Z., Wang, H., Cheng, Y., 2022. Investigation into the adsorption of CO<sub>2</sub>, N<sub>2</sub> and CH<sub>4</sub> on kaolinite clay. *Arab. J. Chem.* 15 (3), 103665. <http://dx.doi.org/10.1016/j.arabjc.2021.103665>.
- Duan, S., Gu, M., Du, X., Xian, X., 2016. Adsorption equilibrium of CO<sub>2</sub> and CH<sub>4</sub> and their mixture on Sichuan Basin shale. *Energy Fuels* 30 (3), 2248–2256. <http://dx.doi.org/10.1021/acs.energyfuels.5b02088>.
- Etminan, S.R., Javadpour, F., Maini, B.B., Chen, Z., 2014. Measurement of gas storage processes in shale and of the molecular diffusion coefficient in kerogen. *Int. J. Coal Geol.* 123, 10–19. <http://dx.doi.org/10.1016/j.coal.2013.10.007>.
- Fan, K., Li, Y., Elsworth, D., Dong, M., Yin, C., Li, Y., Chen, Z., 2018. Three stages of methane adsorption capacity affected by moisture content. *Fuel* 231, 352–360. <http://dx.doi.org/10.1016/j.fuel.2018.05.120>.
- Fatah, A., Ben Mahmud, H., Bennour, Z., Gholami, R., Hossain, M., 2022a. The impact of supercritical CO<sub>2</sub> on the pore structure and storage capacity of shales. *J. Nat. Gas Sci. Eng.* 98, 104394. <http://dx.doi.org/10.1016/j.jngse.2021.104394>.
- Fatah, A., Mahmud, H.B., Bennour, Z., Gholami, R., Hossain, M.M., 2022. Geochemical and physical alteration of clay-rich shales under supercritical CO<sub>2</sub> conditions. *Appl. Geochem.* 140, 105291. <http://dx.doi.org/10.1016/j.apgeochem.2022.105291>.
- Fatah, A., Mahmud, H.B., Bennour, Z., Hossain, M., Gholami, R., 2021. Effect of supercritical CO<sub>2</sub> treatment on physical properties and functional groups of shales. *Fuel* 303, 121310. <http://dx.doi.org/10.1016/j.fuel.2021.121310>.
- Fathi, E., Akkutlu, I.Y., 2014. Multi-component gas transport and adsorption effects during CO<sub>2</sub> injection and enhanced shale gas recovery. *Int. J. Coal Geol.* 123, 52–61. <http://dx.doi.org/10.1016/j.coal.2013.07.021>.
- Fu, H., Yan, D., Yao, C., et al., 2022. Pore structure and multi-scale fractal characteristics of adsorbed pores in marine shale: A case study of the lower silurian longmaxi shale in the Sichuan Basin, China. *J. Earth Sci.* 33, 1278–1290. <http://dx.doi.org/10.1007/s12583-021-1602-0>.
- Gasparik, M., Bertier, P., Gensterblum, Y., Ghanizadeh, A., Krooss, B.M., Littke, R., 2014. Geological controls on the methane storage capacity in organic-rich shales. *Int. J. Coal Geol.* 123, 34–51. <http://dx.doi.org/10.1016/j.coal.2013.06.010>.
- Gregg, S.J., Sing, K.S.W., Salzberg, H., 1967. Adsorption surface area and porosity. *J. Electrochem. Soc.* 114 (11), 279Ca. [http://dx.doi.org/10.1016/0021-9797\(83\)90305-3](http://dx.doi.org/10.1016/0021-9797(83)90305-3).

- Groen, J.C., Peffer, L.A., Pérez-Ramírez, J., 2003. Pore size determination in modified micro- and mesoporous materials. Pitfalls and limitations in gas adsorption data analysis. *Microporous Mesoporous Mater.* 60 (1–3), 1–17. [http://dx.doi.org/10.1016/S1387-1811\(03\)00339-1](http://dx.doi.org/10.1016/S1387-1811(03)00339-1).
- Gu, Y., Ding, W., Yin, S., Yin, M., Xiao, Z., 2018. Adsorption characteristics of clay minerals in shale. *Pet. Sci. Technol.* 36 (2), 108–114. <http://dx.doi.org/10.1080/10916466.2017.1405031>.
- Gu, Y., Wan, Q., Li, X., Han, T., Yang, S., Hu, Q., 2023. Structure and evolution of clay-organic nanocomposites in three leading shales in China. *J. Earth Sci.* <http://dx.doi.org/10.1007/s12583-022-1717-y>.
- Guo, X., Hu, D., Li, Y., Wei, Z., Wei, X., Liu, Z., 2017. Geological factors controlling shale gas enrichment and high production in fuling shale gas field. *Pet. Explor. Dev.* 44 (4), 513–523. [http://dx.doi.org/10.1016/S1876-3804\(17\)30060-5](http://dx.doi.org/10.1016/S1876-3804(17)30060-5).
- Han, Y., Chen, S., Zhu, Y., Zhou, S., 2017. Micro and nano-size pore characteristics of clay minerals in a shale reservoir of the Longmaxi formation in the middle and Upper Yangtze Area, China. *J. Nanosci. Nanotechnol.* 17 (9), 6508–6517. <http://dx.doi.org/10.1166/jnn.2017.14422>.
- Hao, F., Zou, H., Lu, Y., 2013. Mechanisms of shale gas storage: Implications for shale gas exploration in China. *AAPG Bull.* 97 (8), 1325–1346. <http://dx.doi.org/10.1306/02141312091>.
- Hatch, C.D., Wiese, J.S., Crane, C.C., Harris, K.J., Kloss, H.G., Baltrusaitis, J., 2012. Water adsorption on clay minerals as a function of relative humidity: application of BET and freundlich adsorption models. *Langmuir* 28 (3), 1790–1803. <http://dx.doi.org/10.1021/la2042873>.
- Hayati-Ashtiani, M., 2011. Characterization of nano-porous bentonite (montmorillonite) particles using FTIR and BET-BJH analyses. *Part. Part. Syst. Charact.* 28 (3–4), 71–76. <http://dx.doi.org/10.1002/ppsc.201100030>.
- Helgeson, H.C., Richard, L., McKenzie, W.F., Norton, D.L., Schmitt, A., 2009. A chemical and thermodynamic model of oil generation in hydrocarbon source rocks. *Geochim. Cosmochim. Acta* 73 (3), 594–695. <http://dx.doi.org/10.1016/j.gca.2008.03.004>.
- Heller, R., Zoback, M., 2014. Adsorption of methane and carbon dioxide on gas shale and pure mineral samples. *J. Unconv. Oil Gas Resour.* 8, 14–24. <http://dx.doi.org/10.1016/j.juogr.2014.06.001>.
- Hu, N., 2018. *Adsorption Characteristics of Supercritical CH<sub>4</sub> and CO<sub>2</sub> in Shale*. Chongqing University.
- Hu, Z., Gaus, G., Seemann, T., Zhang, Q., Littke, R., Fink, R., 2021a. Pore structure and sorption capacity investigations of Ediacaran and Lower Silurian gas shales from the Upper Yangtze platform, China. *Geomech. Geophys. Geo-Energy Geo-Resour.* 7 (3), 1–26. <http://dx.doi.org/10.1007/s40948-021-00262-5>.
- Hu, Z., Lu, S., Klaver, J., Dewanckele, J., Amann-Hildenbrand, A., Gaus, G., Littke, R., 2021b. An integrated imaging study of the pore structure of the Cobourg limestone—A potential nuclear waste host rock in Canada. *Minerals* 11 (10), 1042. <http://dx.doi.org/10.3390/min11101042>.
- Hu, Y., Pan, X., Han, X., Bao, X., 2017. Displacement and diffusion of methane and carbon dioxide in SBA-15 studied by NMR. *J. Phys. Chem. C* 121 (4), 2481–2486. <http://dx.doi.org/10.1021/acs.jpcc.6b12250>.
- Huang, Z., Liu, G., Li, T., Li, Y., Yin, Y., Wang, L., 2017. Characterization and control of mesopore structural heterogeneity for low thermal maturity shale: A case study of Yanchang Formation Shale, Ordos Basin. *Energy Fuels* 31 (11), 11569–11586. <http://dx.doi.org/10.1021/acs.energyfuels.7b01414>.
- Huang, X., Zhao, Y.-P., Wang, X., Pan, L., 2019. Adsorption-induced pore blocking and its mechanisms in nanoporous shale due to interactions with supercritical CO<sub>2</sub>. *J. Pet. Sci. Eng.* 178, 74–81. <http://dx.doi.org/10.1016/j.petrol.2019.03.018>.
- Hui, D., Pan, Y., Luo, P., Zhang, Y., Sun, L., Lin, C., 2019. Effect of supercritical CO<sub>2</sub> exposure on the high-pressure CO<sub>2</sub> adsorption performance of shales. *Fuel* 247, 57–66. <http://dx.doi.org/10.1016/j.fuel.2019.03.013>.
- Jarboe, P.J., Candela, P.A., Zhu, W., Kaufman, A.J., 2015. Extraction of hydrocarbons from high-maturity marcellus shale using supercritical carbon dioxide. *Energy Fuels* 29 (12), 7897–7909. <http://dx.doi.org/10.1021/acs.energyfuels.5b02059>.
- Ji, L., Zhang, T., Milliken, K.L., Qu, J., Zhang, X., 2012. Experimental investigation of main controls to methane adsorption in clay-rich rocks. *Appl. Geochem.* 27 (12), 2533–2545. <http://dx.doi.org/10.1016/j.apgeochem.2012.08.027>.
- Jiang, H., Daigle, H., Milliken, K.L., Hayman, N.W., 2019. Porosity-deformation relationships in organic-rich shale. In: *AAPG Memoir*. pp. 149–164. <http://dx.doi.org/10.1306/13672215M1213825>.
- Jiang, Y., Luo, Y., Lu, Y., Qin, C., Liu, H., 2016. Effects of supercritical CO<sub>2</sub> treatment time, pressure, and temperature on microstructure of shale. *Energy* 97, 173–181. <http://dx.doi.org/10.1016/j.energy.2015.12.124>.
- Kendall, J.L., Canelas, D.A., Young, J.L., DeSimone, J.M., 1999. Polymerizations in supercritical carbon dioxide. *Chem. Rev.* 99, 543–564. <http://dx.doi.org/10.1021/cr9700336>.
- Klewiah, I., Berawala, D.S., Alexander Walker, H.C., Andersen, P.Ø., Nadeau, P.H., 2020. Review of experimental sorption studies of CO<sub>2</sub> and CH<sub>4</sub> in shales. *J. Nat. Gas Sci. Eng.* 73, 103045. <http://dx.doi.org/10.1016/j.jngse.2019.103045>.
- Krooss, B.v., Van Bergen, F., Gensterblum, Y., Siemons, N., Pagnier, H., David, P., 2002. High-pressure methane and carbon dioxide adsorption on dry and moisture-equilibrated Pennsylvanian coals. *Int. J. Coal Geol.* 51 (2), 69–92. [http://dx.doi.org/10.1016/S0166-5162\(02\)00078-2](http://dx.doi.org/10.1016/S0166-5162(02)00078-2).
- Kweon, H., Deo, M., 2017. The impact of reactive surface area on brine-rock-carbon dioxide reactions in CO<sub>2</sub> sequestration. *Fuel* 188, 39–49. <http://dx.doi.org/10.1016/j.fuel.2016.10.010>.
- Lan, Y., Yang, Z., Wang, P., Yan, Y., Zhang, L., Ran, J., 2019. A review of microscopic seepage mechanism for shale gas extracted by supercritical CO<sub>2</sub> flooding. *Fuel* 238, 412–424. <http://dx.doi.org/10.1016/j.fuel.2018.10.130>.
- Langmuir, I., 1916. The constitution and fundamental properties of solids and liquids. Part I. Solids. *J. Am. Chem. Soc.* 38 (11), 2221–2295. <http://dx.doi.org/10.1021/ja02268a002>.
- Langmuir, I., 1918. The adsorption of gases on plane surfaces of glass, mica and platinum. *J. Am. Chem. Soc.* 40 (9), 1361–1403. <http://dx.doi.org/10.1021/ja02242a004>.
- Li, A., Ding, W., Zhou, X., Cao, X., Zhang, M., Fu, F., Chen, E., 2017a. Investigation of the methane adsorption characteristics of marine shale: a case study of Lower Cambrian Qiongzhusi Shale in eastern Yunnan Province, South China. *Energy Fuels* 31 (3), 2625–2635. <http://dx.doi.org/10.1021/acs.energyfuels.6b03168>.
- Li, J., Kuppler, R.J., Zhou, H., 2009. Selective gas adsorption and separation in metal-organic frameworks. *Chem. Soc. Rev.* 38 (5), 1477–1504. <http://dx.doi.org/10.1039/b802426j>.
- Li, X., Wang, Y., Lin, W., Ma, L., Liu, D., Liu, J., Zhang, Y., 2022. Micro-pore structure and fractal characteristics of deep shale from Wufeng formation to Longmaxi formation in Jingmen exploration area, Hubei Province, China. *J. Nat. Gas Geosci.* 7 (3), 121–132. <http://dx.doi.org/10.1016/j.jnggs.2022.06.001>.
- Li, Y., Wang, Y., Wang, J., Pan, Z., 2020a. Variation in permeability during CO<sub>2</sub>-CH<sub>4</sub> displacement in coal seams: part 1—experimental insights. *Fuel* 263, 116666. <http://dx.doi.org/10.1016/j.fuel.2019.116666>.
- Li, Y., et al., 2020b. Nanoscale pore structure and mechanical property analysis of coal: An insight combining AFM and SEM images. *Fuel* 260, 116352. <http://dx.doi.org/10.1016/j.fuel.2019.116352>.
- Liao, Q., Zhou, J., Xian, X., Yang, K., Zhang, C., Dong, Z., Yin, H., 2023. Competition adsorption of CO<sub>2</sub>/CH<sub>4</sub> in shale: Implications for CO<sub>2</sub> sequestration with enhanced gas recovery. *Fuel* 339, 127400. <http://dx.doi.org/10.1016/j.fuel.2023.127400>.
- Liu, Q., 2017. *Study on the Influence of Supercritical CO<sub>2</sub> Treatment on the Microstructure and CH<sub>4</sub>/CO<sub>2</sub> Adsorption Characteristics of Shale*. Chongqing University.
- Liu, S., Sun, B., Xu, J., Li, H., Wang, X., 2020. Study on competitive adsorption and displacing properties of CO<sub>2</sub> enhanced shale gas recovery: advances and challenges. *Geofluids* 2020. <http://dx.doi.org/10.1155/2020/6657995>.
- Lu, Y., Ao, X., Tang, J., Jia, Y., Zhang, X., Chen, Y., 2016. Swelling of shale in supercritical carbon dioxide. *J. Nat. Gas Sci. Eng.* 30, 268–275. <http://dx.doi.org/10.1016/j.jngse.2016.02.011-PA>.
- Lu, X.-C., Li, F.-C., Watson, A.T., 1995. Adsorption studies of natural gas storage in Devonian shales. *SPE Form. Eval.* 10 (02), 109–113. <http://dx.doi.org/10.2118/26632>.
- Lu, Y., Zhou, J., Xian, X., Tang, J., Zhou, L., Jiang, Y., 2021. Progress and prospects of integrated research on supercritical CO<sub>2</sub>-enhanced shale gas extraction and geological storage. *Nat. Gas Ind.* 41 (6), <http://dx.doi.org/10.3787/j.issn.1000-0976.2021.06.007>.
- Luo, X., Wang, S., Wang, Z., Jing, Z., Lv, M., Zhai, Z., Han, T., 2015. Adsorption of methane, carbon dioxide and their binary mixtures on Jurassic shale from the Qaidam Basin in China. *Int. J. Coal Geol.* 150, 210–223. <http://dx.doi.org/10.1016/j.coal.2015.09.004>.
- Lutyński, M., Waszczuk, P., Słomski, P., Szczepański, J., 2017. CO<sub>2</sub> sorption of Pomeranian gas bearing shales—the effect of clay minerals. *Energy Procedia* 125, 457–466. <http://dx.doi.org/10.1016/j.egypro.2017.08.153>.
- Mastalerz, M., Rupp, J., Drobnik, A., Harpalani, S., Anderson, A., Korose, C., Frailey, S., Morse, D., 2009. Assessment of CO<sub>2</sub> Sequestration and Enhanced Coalbed Methane Potential in Unminable Coal Seams of the Illinois Basin. In: *AAPG Studies in Geology*, pp. 457–474. <http://dx.doi.org/10.1306/131712385593380>.
- Mattia, D., Starov, V., Semenov, S., 2012. Thickness, stability and contact angle of liquid films on and inside nanofibres, nanotubes and nanochannels. *J. Colloid Interface Sci.* 384 (1), 149–156. <http://dx.doi.org/10.1016/j.jcis.2012.06.051>.
- Mery, S., Sinayuc, C., 2018. Adsorption behaviour of shale gas reservoirs. *Int. J. Oil Gas Coal Technol.* 17 (2), 172–188. <http://dx.doi.org/10.1504/ijogct.2018.089941>.
- Mudoi, M.P., Sharma, P., Khichi, A.S., 2022. A review of gas adsorption on shale and the influencing factors of CH<sub>4</sub> and CO<sub>2</sub> adsorption. *J. Pet. Sci. Eng.* 217, 110897. <http://dx.doi.org/10.1016/j.petrol.2022.110897>.
- Nelson, P.H., 2009. Pore-throat sizes in sandstones, tight sandstones, and shales. *AAPG Bull.* 93 (3), 329–340. <http://dx.doi.org/10.1306/10240808059>.
- Nie, B., Liu, X., Yang, L., Meng, J., Li, X., 2015. Pore structure characterization of different rank coals using gas adsorption and scanning electron microscopy. *Fuel* 158, 908–917. <http://dx.doi.org/10.1016/j.fuel.2015.06.050>.

- Niu, Y., Yue, C., Li, S., Ma, Y., Xu, X., 2018. Influencing factors and selection of CH<sub>4</sub> and CO<sub>2</sub> adsorption on Silurian shale in Yibin, Sichuan province of China. *Energy Fuels* 32 (3), 3202–3210. <http://dx.doi.org/10.1021/acs.energyfuels.7b03815>.
- Norman, C., 1974. Huge resources needed to exploit shale oil. *Nature* 249 (5459), 704–706. <http://dx.doi.org/10.1038/249704a0>.
- Nuttall, B.C., Eble, C., Bustin, R.M., Drahovzal, J.A., 2005. Analysis of devonian black shales in Kentucky for potential carbon dioxide sequestration and enhanced natural gas production. In: *Greenhouse Gas Control Technologies, Vol. 7*. Elsevier, pp. 2225–2228.
- Nuttall, B.C., Drahovzal, J.A., Eble, C.F., Bustin, R.M., 2009. Regional Assessment of Suitability of Organic-Rich Gas Shales for Carbon Sequestration: an Example from the Devonian Shales of the Illinois and Appalachian Basins, Kentucky. In: *AAPG Studies in Geology*, vol. 59, pp. 173–190. <http://dx.doi.org/10.1306/13171239St593381>.
- Orr, C., Kolthoff, I., Elving, P., Stross, F., 1977. Pore size and volume measurement. In: *Treatise on Analytical Chemistry Part III, Vol. 4*. John Wiley and Sons, New York, pp. 321–358.
- Pan, Y., Hui, D., Luo, P., Zhang, Y., Sun, L., Wang, K., 2018a. Experimental investigation of the geochemical interactions between supercritical CO<sub>2</sub> and shale: Implications for CO<sub>2</sub> storage in gas-bearing shale formations. *Energy Fuels* 32 (2), 1963–1978. <http://dx.doi.org/10.1021/acs.energyfuels.7b03074>.
- Pan, Y., Hui, D., Luo, P., Zhang, Y., Zhang, L., Sun, L., 2018b. Influences of subcritical and supercritical CO<sub>2</sub> treatment on the pore structure characteristics of marine and terrestrial shales. *J. CO<sub>2</sub> Util.* 28, 152–167. <http://dx.doi.org/10.1016/j.jcou.2018.09.016>.
- Pathak, M., Huang, H., Meakin, P., Deo, M., 2018. Molecular investigation of the interactions of carbon dioxide and methane with kerogen: Application in enhanced shale gas recovery. *J. Nat. Gas Sci. Eng.* 51, 1–8. <http://dx.doi.org/10.1016/j.jngse.2017.12.021>.
- Peng, C., Crawshaw, J.P., Maitland, G.C., Trusler, J.M., Vega-Maza, D., 2013. The pH of CO<sub>2</sub>-saturated water at temperatures between 308 K and 423 K at pressures up to 15 MPa. *J. Supercrit. Fluids* 82, 129–137. <http://dx.doi.org/10.1016/j.supflu.2013.07.001>.
- Pfeifer, P., Avnir, D., 1983. Chemistry in noninteger dimensions between two and three. I. Fractal theory of heterogeneous surfaces. *J. Chem. Phys.* 79 (7), 3558–3565. <http://dx.doi.org/10.1063/1.446210>.
- Pozo, M., Pino, D., Bessieres, D., 2017. Effect of thermal events on maturation and methane adsorption of Silurian black shales (Checa, Spain). *Appl. Clay Sci.* 136, 208–218. <http://dx.doi.org/10.1016/j.clay.2016.11.026>.
- Pusch, A.-K., Splith, T., Moschkowitz, L., Karmakar, S., Biniwale, R., Sant, M., Suffritti, G.B., Demontis, P., Cravillon, J., Pantatosaki, E., 2012. NMR studies of carbon dioxide and methane self-diffusion in ZIF-8 at elevated gas pressures. *Adsorption* 18 (5), 359–366. <http://dx.doi.org/10.1007/s10450-012-9414-2>.
- Qi, R., Ning, Z., Wang, Q., Zeng, Y., Huang, L., Zhang, S., Du, H., 2018. Sorption of methane, carbon dioxide, and their mixtures on shales from Sichuan Basin, China. *Energy Fuels* 32 (3), 2926–2940. <http://dx.doi.org/10.1021/acs.energyfuels.7b03429>.
- Qin, C., Jiang, Y., Luo, Y., Xian, X., Liu, H., Li, Y., 2016. Effect of supercritical carbon dioxide treatment time, pressure, and temperature on shale water wettability. *Energy Fuels* 31 (1), 493–503. <http://dx.doi.org/10.1021/acs.energyfuels.6b03257>.
- Rani, S., Prusty, B.K., Padmanabhan, E., Pal, S.K., 2019. Applicability of various adsorption isotherm models on adsorption of methane and CO<sub>2</sub> on Indian shales. *Environ. Prog. Sustain. Energy* 38 (6), 13222. <http://dx.doi.org/10.1002/ep.13222>.
- Ren, W., Li, G., Tian, S., Sheng, M., Geng, L., 2017. Adsorption and surface diffusion of supercritical methane in shale. *Ind. Eng. Chem. Res.* 56 (12), 3446–3455. <http://dx.doi.org/10.1021/acs.iecr.6b04432>.
- Rexer, T.F., Mathia, E.J., Aplin, A.C., Thomas, K.M., 2014. High-pressure methane adsorption and characterization of pores in Posidonia shales and isolated kerogens. *Energy Fuels* 28 (5), 2886–2901. <http://dx.doi.org/10.1021/ef402466m>.
- Rezaee, R., Saeedi, A., Iglauer, S., Evans, B., 2017. Shale alteration after exposure to supercritical CO<sub>2</sub>. *Int. J. Greenh. Gas Control* 62, 91–99. <http://dx.doi.org/10.1016/j.jggc.2017.04.004>.
- Rogala, A., Ksiezniak, K., Krzysiek, J., Hupka, J., 2014. Carbon dioxide sequestration during shale gas recovery. *Physicochem. Probl. Miner. Process.* 50, <http://dx.doi.org/10.5277/ppmp140221>.
- Sakurovs, R., Day, S., Weir, S., Duffy, G., 2007. Application of a modified Dubinin–Radushkevich equation to adsorption of gases by coals under supercritical conditions. *Energy Fuels* 21 (2), 992–997. <http://dx.doi.org/10.1021/ef0600614>.
- Sanguinito, S., Goodman, A., Tkach, M., Kutchko, B., Culp, J., Natesakhawat, S., Fazio, J., Fukai, I., Crandall, D., 2018. Quantifying dry supercritical CO<sub>2</sub>-induced changes of the Utica shale. *Fuel* 226, 54–64. <http://dx.doi.org/10.1016/j.fuel.2018.03.156>.
- Schaeff, H.T., Davidson, C.L., Owen, A.T., Miller, Q.R., Loring, J.S., Thompson, C.J., Bacon, D.H., Glezakou, V.A., McGrail, B.P., 2014a. CO<sub>2</sub> utilization and storage in shale gas reservoirs: experimental results and economic impacts. *Energy Procedia* 63, 7844–7851. <http://dx.doi.org/10.1016/j.egypro.2014.11.819>.
- Schaeff, H.T., Glezakou, V.-A., Owen, A.T., Ramprasad, S., Martin, P.F., McGrail, B.P., 2014b. Surface condensation of CO<sub>2</sub> onto kaolinite. *Environ. Sci. Technol. Lett.* 1 (2), 142–145. <http://dx.doi.org/10.1021/ez400169b>.
- Sondergeld, C.H., Ambrose, R.J., Rai, C.S., Moncrieff, J., 2010. Micro-structural studies of gas shales. In: *SPE Unconventional Gas Conference*. OnePetro.
- Sondergeld, C.H., Rai, C.S., Curtis, M.E., 2013. Microstructure and anisotropy in gas shales. In: *AAPG Memoir, Vol. 105*, pp. 179–187.
- Strubinger, J.R., Song, H., Parcher, J.F., 1991. High-pressure phase distribution isotherms for supercritical fluid chromatographic systems. 1. Pure carbon dioxide. *Anal. Chem.* 63 (2), 98–103. <http://dx.doi.org/10.1021/ac00002a003>.
- Sui, H., Yao, J., 2016. Molecular simulation of CO<sub>2</sub>/CH<sub>4</sub> competitive adsorption in kerogen. *J. China Univ. Pet.* 40 (2), 147–154. <http://dx.doi.org/10.3969/j.issn.1673-5005.2016.02.019>.
- Sun, L., Gao, Y., Pan, Y., Ou, C., 2017. Surface fractal characteristics and their influence on shale nanopores. *J. Southwest Petrol. Univ.* 39 (6), 85. <http://dx.doi.org/10.11885/j.issn.1674-5086.2016.11.03.30>.
- Sun, Z., He, Z., Wang, F., Han, Y., He, S., Hou, Y., Luo, J., Zheng, Y., Wu, S., 2022. Occurrence characteristics of saline-lacustrine shale-oil in the Qianjiang Depression, Jiangnan Basin, Central China. *J. Earth Sci.* 33, 945–962. <http://dx.doi.org/10.1007/s12583-020-1110-7>.
- Sun, M., Zhao, J., Pan, Z., Hu, Q., Yu, B., Tan, Y., Sun, L., Bai, L., Wu, C., Blach, T.P., 2020. Pore characterization of shales: A review of small angle scattering technique. *J. Nat. Gas Sci. Eng.* 78, 103294. <http://dx.doi.org/10.1016/j.jngse.2020.103294>.
- Tang, X., Ripepi, N., Luxbacher, K., Pitcher, E., 2017. Adsorption models for methane in shales: Review, comparison, and application. *Energy Fuels* 31 (10), 10787–10801. <http://dx.doi.org/10.1021/acs.energyfuels.7b01948>.
- Tao, Y., Lianbo, Z., Haikuan, N., 2019. Adsorption capacity and controlling factors of marine-continental transitional shale in Xiangzhong depression. *Lithol. Reserv.* 31 (2), 105–114. <http://dx.doi.org/10.12108/xyqc.20190212>.
- Thomas, M., Partridge, T., Harthorn, B.H., Pidgeon, N., 2017. Deliberating the perceived risks, benefits, and societal implications of shale gas and oil extraction by hydraulic fracturing in the US and UK. *Nature Energy* 2 (5), 1–7. <http://dx.doi.org/10.1038/nenergy.2017.54>.
- Thommes, M., Kaneko, K., Neimark, A.V., Olivier, J.P., Rodriguez-Reinoso, F., Rouquerol, J., Sing, K.S., 2015. Physisorption of gases, with special reference to the evaluation of surface area and pore size distribution. *Pure Appl. Chem.* 87 (9–10), 1051–1069. <http://dx.doi.org/10.1515/ci-2016-0119>, IUPAC Technical Report.
- Ujiié, Y., 1978. Kerogen maturation and petroleum genesis. *Nature* 272 (5652), 438–439. <http://dx.doi.org/10.1038/272438a0>.
- Wang, Z., Krupnick, A., 2015. A retrospective review of shale gas development in the United States: What led to the boom? *Econ. Energy Environ. Policy* 4 (1), 5–18. <http://dx.doi.org/10.5547/2160-5890.4.1.zwan>.
- Wang, H., Li, G., Shen, Z., 2012. A feasibility analysis on shale gas exploitation with supercritical carbon dioxide. *Energy Sources Part A: Recovery Util. Environ. Eff.* 34 (15), 1426–1435. <http://dx.doi.org/10.1080/15567036.2010.529570>.
- Wei, M., Xiong, Y., Zhang, L., Li, J., 2016. The effect of sample particle size on the determination of pore structure parameters in shales. *Int. J. Coal Geol.* 163, 177–185. <http://dx.doi.org/10.1016/j.coal.2016.07.013>.
- Welte, D., Tissot, P., 1984. *Petroleum Formation and Occurrence*. Springer.
- Weniger, P., Kalkreuth, W., Busch, A., Krooss, B.M., 2010. High-pressure methane and carbon dioxide sorption on coal and shale samples from the Paraná Basin, Brazil. *Int. J. Coal Geol.* 84 (3–4), 190–205. <http://dx.doi.org/10.1016/j.coal.2010.08.003>.
- Yang, J., Lian, H., Li, L., 2020. Fracturing in coals with different fluids: an experimental comparison between water, liquid CO<sub>2</sub>, and supercritical CO<sub>2</sub>. *Sci. Rep.* 10 (1), 1–15. <http://dx.doi.org/10.1038/s41598-020-75787-y>.
- Yang, F., Ning, Z., Zhang, R., Zhao, H., Krooss, B.M., 2015. Investigations on the methane sorption capacity of marine shales from Sichuan Basin, China. *Int. J. Coal Geol.* 146, 104–117. <http://dx.doi.org/10.1016/j.coal.2015.05.009>.
- Yang, K., Zhou, J., Xian, X., Jiang, Y., Zhang, C., Lu, Z., Yin, H., 2022a. Gas adsorption characteristics changes in shale after supercritical CO<sub>2</sub>-water exposure at different pressures and temperatures. *Fuel* 310, 122260. <http://dx.doi.org/10.1016/j.fuel.2021.122260>.
- Yang, Z., Zou, C., Wu, S., Pan, S., Wang, X., Liu, H., Jiang, W., Li, J., Li, Q., Niu, X., Li, G., Tang, Z., Guo, X., Huang, D., Wei, Q., 2022b. Characteristics, types, and prospects of geological sweet sections in giant continental shale oil provinces in China. *J. Earth Sci.* 33, 1260–1277. <http://dx.doi.org/10.1007/s12583-022-1735-9>.
- Yin, H., Zhou, J., Jiang, Y., Xian, X., Liu, Q., 2016. Physical and structural changes in shale associated with supercritical CO<sub>2</sub> exposure. *Fuel* 184, 289–303. <http://dx.doi.org/10.1016/j.fuel.2016.07.028>.
- Zhang, T., Ellis, G.S., Ruppel, S.C., Milliken, K., Yang, R., 2012. Effect of organic-matter type and thermal maturity on methane adsorption in shale-gas systems. *Org. Geochem.* 47, 120–131. <http://dx.doi.org/10.1016/j.orggeochem.2012.03.012>.
- Zhao, J., Ren, L., Jiang, T., Hu, D., Wu, L., Wu, J., Yin, C., Li, Y., Hu, Y., Lin, R., 2022a. Ten years of gas shale fracturing in China: review and prospect. *Nat. Gas Ind. B* 9 (2), 158–175. <http://dx.doi.org/10.1016/j.ngib.2022.03.002>.

- Zhao, W., Su, X., Xia, D., Hou, S., Wang, Q., Zhou, Y., 2022b. Enhanced coalbed methane recovery by the modification of coal reservoir under the supercritical CO<sub>2</sub> extraction and anaerobic digestion. *Energy* 259, 124914. <http://dx.doi.org/10.1016/j.energy.2022.124914>.
- Zhao, G., Wang, C., 2019. Influence of CO<sub>2</sub> on the adsorption of CH<sub>4</sub> on shale using low-field nuclear magnetic resonance technique. *Fuel* 238, 51–58. <http://dx.doi.org/10.1016/j.fuel.2018.10.092>.
- Zheng, S., Yao, Y., Liu, D., Cai, Y., Liu, Y., 2018. Characterizations of full-scale pore size distribution, porosity and permeability of coals: A novel methodology by nuclear magnetic resonance and fractal analysis theory. *Int. J. Coal Geol.* 196, 148–158. <http://dx.doi.org/10.1016/j.coal.2018.07.008>.
- Zheng, S., Yao, Y., Liu, D., Cai, Y., Liu, Y., Li, X., 2019. Nuclear magnetic resonance T2 cutoffs of coals: A novel method by multifractal analysis theory. *Fuel* 241, 715–724. <http://dx.doi.org/10.1016/j.fuel.2018.12.044>.
- Zhou, J., Fan, M., Xian, X., Yang, K., Lu, Z., 2022a. Correction calculation of shale gas absolute adsorption capacity and its influencing factors analysis. *Coal Sci. Technol.* 50 (2), 154–162. <http://dx.doi.org/10.13199/j.cnki.cst.2021-0715>.
- Zhou, S., Liu, H., Chen, H., Wang, H., Guo, W., Liu, D., Zhang, Q., Wu, J., Shen, W., 2019a. A comparative study of the nanopore structure characteristics of coals and longmaxi shales in China. *Energy Sci. Eng.* 7 (6), 2768–2781. <http://dx.doi.org/10.1002/ese3.458>.
- Zhou, J., Liu, M., Xian, X., Jiang, Y., Liu, Q., Wang, X., 2019b. Measurements and modelling of CH<sub>4</sub> and CO<sub>2</sub> adsorption behaviors on shales: Implication for CO<sub>2</sub> enhanced shale gas recovery. *Fuel* 251, 293–306. <http://dx.doi.org/10.1016/j.fuel.2019.04.041>.
- Zhou, J., Tian, S., Yang, K., Dong, Z., Cai, J., 2022b. Enhanced gas recovery technologies aimed at exploiting captured carbon dioxide. In: *Sustainable Natural Gas Reservoir and Production Engineering*. Elsevier, pp. 305–347. <http://dx.doi.org/10.1016/B978-0-12-824495-1.00010-3>.
- Zhou, J., Xie, S., Jiang, Y., Xian, X., Liu, Q., Lu, Z., Lyu, Q., 2018a. Influence of supercritical CO<sub>2</sub> exposure on CH<sub>4</sub> and CO<sub>2</sub> adsorption behaviors of shale: implications for CO<sub>2</sub> sequestration. *Energy Fuels* 32 (5), 6073–6089. <http://dx.doi.org/10.1021/acs.energyfuels.8b00551>.
- Zhou, S., Xue, H., Ning, Y., Guo, W., Zhang, Q., 2018b. Experimental study of supercritical methane adsorption in Longmaxi shale: Insights into the density of adsorbed methane. *Fuel* 211, 140–148. <http://dx.doi.org/10.1016/j.fuel.2017.09.065>.
- Zou, C., He, D., Jia, C., Xiong, B., Zhao, Q., Pan, S., 2021. Connotation and pathway of world energy transition and its significance for carbon neutral. *Acta Petrolei Sin.* 42 (2), 233–247. <http://dx.doi.org/10.7623/syxb202102008>.
- Zou, J., Rezaee, R., Liu, K., 2017. Effect of temperature on methane adsorption in shale gas reservoirs. *Energy Fuels* 31 (11), 12081–12092. <http://dx.doi.org/10.1021/acs.energyfuels.7b02639>.
- Zou, C., Yang, Z., Li, G., Li, J., Liu, X., Tang, Y., Jiang, T., Yang, Y., Bai, X., Pan, S., Lu, M., Lei, Z., Cai, B., 2022. Why can China realize the continental “shale oil revolution”? *J. Earth Sci.* 33, 1324–1327. <http://dx.doi.org/10.1007/s12583-022-1745-7>.